

## Chapter 4

# Neutral Hydrogen Observations with the Focal L-Band Array for the Green Bank Telescope (FLAG)<sup>1</sup>

### Abstract

A description of the system, observing procedure, data reduction, and preliminary results from commissioning of the Focal L-Band Array for the Green Bank Telescope (FLAG) — a cryogenically cooled 19 dual-polarization phased array feed (PAF) — is presented. Specifically, work related to the commissioning of the HI spectral line mode is presented. Extragalactic HI observed with FLAG compares well with equivalent data taken with the existing GBT single-pixel L-Band feed. The necessary survey time for FLAG to reach an equivalent rms noise levels when compared to similar single-pixel maps is reduced by a factor of five to seven.

## 4.1 Introduction

The increased field-of-view (FOV) provided by phased array feeds (PAFs), and the subsequent increase in survey speed, constitutes the next major advancement in radio astronomy instrumentation. Such arrays have been used commercially for decades (Jeffs et al., 2008), but the unique challenge of operating at extremely low

---

<sup>1</sup>I wish to acknowledge D. J. Pisano, R. Prestage, R. Black, B. Jeffs, M. Ruzindana, M. Burnett, K. Warnick, and A. Roshi as collaborators on this work presented in this chapter.

signal intensities inherent to the detection of astrophysical signals has only recently been overcome (Vilnrotter et al., 1995). Placing densely packed dipole antennas in the focal plane of a radio telescope allows for increased sampling of the incident plane waves of faint astronomical signals. Correlating the generated raw complex voltages and then multiplying by complex coefficients (i.e., beamforming weights) will illuminate the aperture in a manner such that the resulting sky power patterns mimics a multi-beam feed<sup>1</sup> (e.g. Landon et al. 2010; Fisher & Bradley 2000), while avoiding the engineering challenges of positioning physically distinct feeds. This is an especially powerful shortcut for low frequency observations where large physical feeds are necessary that sparsely sample a limited fraction of sky at one instant.

Several PAFs have already been deployed on both large single dishes, such as the 64 m Parkes single dish and aperture synthesis arrays with very encouraging science results. For instance, Reynolds et al. (2017) successfully recreated a detailed neutral hydrogen (HI) column density ( $N_{\text{HI}}$ ) map of the Large Magellanic Cloud originally observed with the Parkes 21cm Multi-beam Receiver, as well as direct HI detections of source from the HI Parkes All-Sky Survey (HIPASS; Barnes et al. 2001) and hydrogen recombination lines. Prototype PAFs for the CSIRO Australian SKA Pathfinder (ASKAP; Heywood et al. 2016) and the nearly APERTIF upgrade to the Westerbork Radio Telescope (WSRT; Oosterloo et al. 2009) have shown excellent capability for wide-field imaging, which will dramatically cut survey speeds.

While the increase in the FOV will be immensely useful on array telescopes

---

<sup>1</sup>A traditional multi-beam receiver packs several distinct feed horns into the focal plane of the telescope.

like the WSRT or ASKAP, such instruments will still suffer from the inherent limitation of missing data in the center of the  $uv$ -plane. The missing short baselines reduce the surface brightness sensitivity by limiting the angular scales over which the instrument is sensitive (Braun & Walterbos, 1985). Single dish observations that contain the missing data for the low spatial frequencies may still be necessary even in the age of the SKA and its precursor array telescopes. The unblocked aperture of the 100m Green Bank Telescope (GBT) reduces the pickup of stray radiation leading to uniform illumination across the primary reflector, meaning potentially unprecedentedly highly sensitive electronically formed beams of a PAF, while also possessing relatively good angular resolution. The potential to decrease the telescope time required for deep ( $N_{\text{HI}} \leq 10^{18} \text{ cm}^{-2}$ ) on-the-fly HI mapping of extended sources HI will make a PAF equipped GBT the ideal instrument to look for previously undetected diffuse HI around nearby galaxies related to potential cold flows (Kereš et al., 2005, 2009).

The Focal L-Band Array for the Green Bank Telescope (FLAG) is a 19 element, dual polarization PAF with cryogenically cooled low noise amplifiers (LNAs) that maximize sensitivity. Previous commissioning observations of this PAF have shown excellent performance in terms of sensitivity and spectral line imaging capabilities (Roshi et al., 2018). In fact, as of Spring 2018, FLAG holds the current world record for the lowest reported system temperature ( $T_{\text{sys}}$ ) normalized by aperture efficiency  $\eta$  at  $25 \pm 3$  K near 1350 MHz for a central beam that is electronically formed (Roshi et al., 2018). This value is on par with the capabilities of the existing single-pixel L-Band receiver. This chapter describes aspects of a new beamforming

backend and discusses the first research quality results and current status of the system. Specifically, the important questions about the system that are explored in this chapter are: over what time scales do the complex beamformer weights begin to degrade? Given similar performance of the two receivers, how well do similar mapping observations explicitly compare between FLAG and the single-pixel feed? What are the comprehensive noise properties of all electronically formed beams and on what time scales (if any) do the noise properties fluctuate? Furthermore, the observations with the PAF discussed in Roshi et al. (2018) were performed with a relatively narrow bandwidth and different polyphase filterbank (PFB) implementation for fine channelization. The focus of this chapter is on FLAG spectral line mapping observations over a variety of extragalactic sources that will clarify some of the remaining questions on the capability of FLAG and the new beamformer that is now in place.

Section 4.2 delves into the theoretical framework of beamforming and the subsequent derivation and application of complex beamformer weights (specifically those that maximize the signal-to-noise); Section 4.3 discusses the specific details of the new production backend; Section 4.4 highlights the specific properties of the calibration and science observations before discussing the custom software package utilized in the calibration and imaging of the these data; Section 1.5 shows the results and examines outstanding questions on performance the performance of FLAG; and Section 1.6 discusses what these latest results mean in the context of the status and future of FLAG as a publicly available instrument on the GBT and its potential scientific contributions.

## 4.2 Theory of Optimal Beamforming

As alluded to Section 1.5, the process of ‘beamforming’ involves the weighted sum of the individual sensor responses to an incident astronomical signal. However, before discussing specific examples and the scientific applications of beamforming, we must first introduce an additional term,  $\mathbf{n}(t)$ , that encapsulates the inherent noise of the system caused, in part, by spillover noise (i.e. the warm ground as seen from the individual sensors (henceforth ‘dipoles’), sky noise from atmospheric and cosmic background radiation, and receiver noise from the front end amplifiers. Such noise can be approximated by an additive zero-mean, time-dependent Gaussian stochastic process. The vector  $n(t)$  is shaped  $M \times 1$  and characterizes the noise in an  $M$  element PAF. The signal model is now of the form as introduced in Landon et al. (2010)

$$\mathbf{z}(t) = \mathbf{a}(\theta)\mathbf{s}(t) + \mathbf{n}(t), \quad (4.1)$$

where  $s(t)$  is also a  $M \times 1$  vector that characterizes the array response (i.e., the recorded complex voltages) in the direction of  $\theta$  to an incident signal. In this application,  $\mathbf{a}(\theta)$  is the  $M \times 1$  array response vector. A dipole response can be multiplied by any complex value,  $w_i$ , in order to change the estimate of  $z_i(t)$ . Extending this to all dipole responses, a new estimate of  $z(t)$  can be found for any particular  $\theta$  by computing a weighted sum of the dipole responses

$$\hat{\mathbf{z}}(t) = \sum_{i=1}^M \mathbf{w}_i^* \mathbf{z}(t) = \mathbf{w}^H \mathbf{z}(t). \quad (4.2)$$

Here,  $\mathbf{w}$  is called the beamforming weight vector that holds the weight for each individual dipole, which effectively alters the aperture illumination pattern seen by that dipole. The  $H$  subscript denotes the Hermitian (complex conjugate transpose) form of the vector. The process of choosing  $\mathbf{w}$  to obtain  $\hat{z}(t)$  is known as ‘beam steering’.

In radio astronomy, where the signals are inherently extremely faint, it is advantageous for an observer to compute weights that maximize the signal-to-noise from a given detection. The individual dipole responses measured over a discrete time sample (i.e., integration) can conveniently be arranged in a covariance matrix

$$\mathbf{R} = \mathbf{z}^H(\mathbf{t})\mathbf{z}(\mathbf{t}), \quad (4.3)$$

where  $\mathbf{R}$  is now an  $M \times M$  matrix of complex values that characterizes the correlations between the recorded complex voltages of the individual dipole elements. Jeffs et al. (2008) goes on to characterize the signal from the array by the equation

$$\mathbf{R} = \mathbf{R}_s + \mathbf{R}_n \quad (4.4)$$

where  $\mathbf{R}_s = \sigma^2 \mathbf{a}(\theta) \mathbf{a}^H(\theta)$  is the signal covariance matrix and  $\mathbf{R}_n$  contains the noise covariance from spillover, background, and the mutual coupling of the dipoles (where a dipole picks up the thermal signatures of the adjacent dipoles).

The noise covariance can be measured by pointing the telescope to a blank patch of sky so that  $\mathbf{z}(\mathbf{t}) \approx \mathbf{n}(\mathbf{t})$ . Equation 4.1 is obtained by pointing at a strong

(> 10 Jy) point source. In this context,  $\mathbf{a}(\theta)$  is the direction vector in the direction,  $\Omega$ . Compute Equation 4.4 for each signal-noise pair of covariance matrices and sum to obtain  $\mathbf{R}$ . The direction vector is explicitly derived by

$$\mathbf{a}(\theta) = \mathbf{R}_n u_{\max}, \quad (4.5)$$

where  $u_{\max}$  is the dominate eigenvector to the generalized eigenvalue equation  $\mathbf{R}u_{\max} = \lambda_{\max}\mathbf{R}_n u_{\max}$ .

Elmer et al. (2012) gives the maximum signal to noise of a beamformer by maximizing the following expression

$$\mathbf{w}_{\max\text{SNR}} = \frac{\mathbf{w}^H \mathbf{R}_s \mathbf{w}}{\mathbf{w}^H \mathbf{R}_n \mathbf{w}}. \quad (4.6)$$

Here, the values contained within the weight vector  $\mathbf{w}$  and its Hermition form are not yet known. The maximization of Equation 4.6 via taking the derivative with respect to  $\mathbf{w}$  and setting the result equal to zero results is effectively finding the dominant eigenvector of the generalized eigenvalue equation

$$\mathbf{R}_s \mathbf{w}_{\max\text{SNR}} = \lambda_{\max} \mathbf{R}_n \mathbf{w}_{\max\text{SNR}}. \quad (4.7)$$

A raw power value  $P$  in units of counts at a particular  $\nu$  and short term integration ( $n$ ) is measured by calculating

$$P_{\nu,n} = \mathbf{w}_{\max\text{SNR},\nu,n}^H \mathbf{R}_{s,\nu,n} \mathbf{w}_{\max\text{SNR},\nu,n}. \quad (4.8)$$

The max-SNR beamforming algorithm manipulates the individual dipole illumination patterns such that the aperture is uniformly illuminated for each formed beam. While this scheme produces the highest gain in a given direction, there is little control over the level of the sidelobes due to sharp transition in illumination pattern (recall that the theory of optics dictates that the far-field beams are related to the aperture illumination via a Fourier Transform). Nevertheless the high sensitivity over a large field of view is particularly advantageous for the detection of diffuse HI. A PAF that simultaneously form beams with reliably low sidelobe structure will decrease the survey times necessary to pursue the detection of cold gas accretion, the study of high velocity clouds (Moss et al., 2013) and the compact clouds being driven from the Galactic center (Di Teodoro et al., 2018).

## 4.3 The FLAG Backend

### 4.3.1 General Overview

The backend for the PAF was developed in collaboration with the Brigham Young University (BYU), West Virginia University (WVU) and the Green Bank Observatory (GBO). It consists of five high performance computing nodes (HPCs), each equipped with two Nvidia GeForce Titan X Graphical Processing Units (GPUs). Each HPC was connected to the Reconfigurable Open Architecture Computing Hardware (ROACH)<sup>2</sup> Field Programmable Gate Arrays (FPGA) boards and received one fifth of the total bandwidth of 151.59 MHz. Each HPC can run in three

---

<sup>2</sup>[https://casper.berkeley.edu/wiki/ROACH-2\\_Revision\\_2](https://casper.berkeley.edu/wiki/ROACH-2_Revision_2)

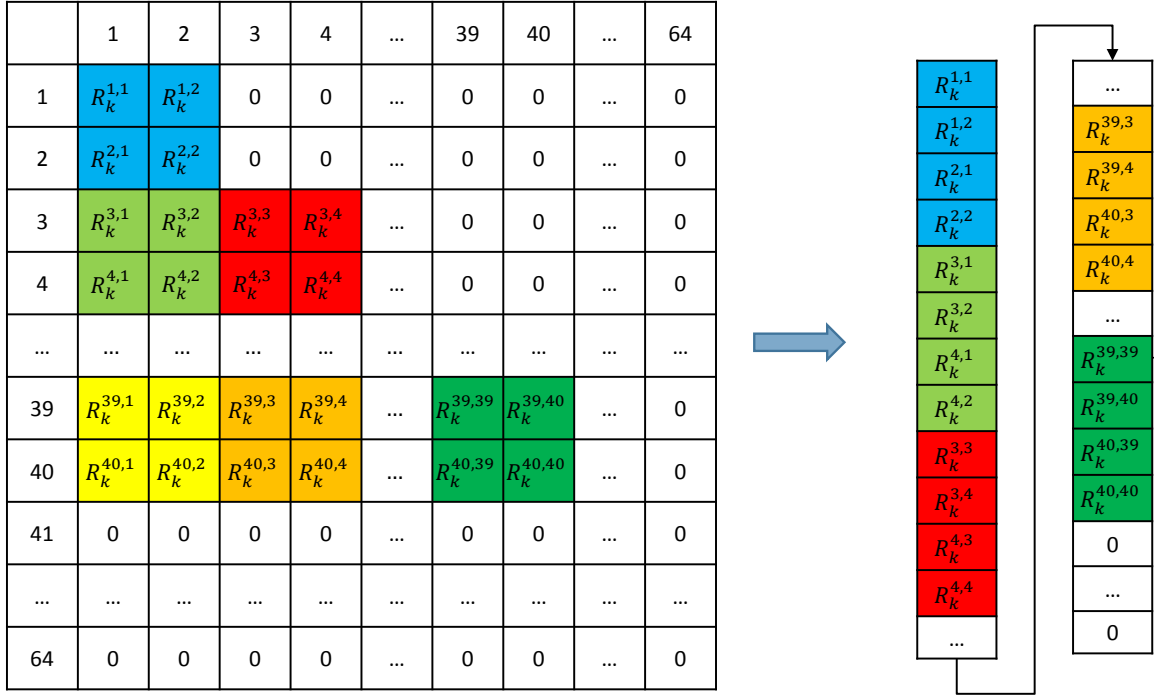


Figure 4.1 The structure of a covariance matrix used in beamforming. The numbers preceding each row/column correspond to the dipole element. Each element of the matrix stores the correlation between dipole elements  $i$  and  $j$  for a single frequency channel,  $k$ . The output is ordered in a flattened one-dimensional array that needs to be reshaped into a  $40 \times 40$  matrix before beamforming weights can be applied. Additionally, due to xGPU limitations, the output size is  $64 \times 64$ , which results in many zeros that need to be thrown away in data processing.

basic modes: (1) the calibration correlator mode (CALCORR) wherein the bandpass was made up of 500 discrete ‘coarse’ channels each 0.30318 MHz wide; (2) The polyphase filter bank (PFB) correlator mode (PFBCORR) where a 30.318 MHz (100 coarse channels) section of the original bandpass is selected to be sent through a PFB to obtain finer channelization. In this mode, a contiguous set of five coarse channels is output to 160 ‘fine’ channels for a final frequency resolution of 9.47 kHz; (3) the real-time beamformer mode (RTBF) where precomputed beamformer weights are read in and applied to save beamformed spectra to disk. This mode is designed to be used to detect transient sources such as pulsars and fast radio bursts. The remaining discussion will focus solely on the CALCORR and the PFBCORR modes.

In both correlator modes, each GPU runs two correlator threads making use of the xGPU library<sup>3</sup>, which is optimized to work on FLAG system parameters. Each correlator thread handles one-twentieth of the total bandwidth made up of either 25 *non-contiguous* coarse frequency channels or 160 contiguous fine channels and writes the raw output to disk in a FITS file format. The data acquisition software used to save these data to disk was borrowed from development code based for the Versatile GBT Astronomical Spectrometer (VEGAS) engineering FITS format. The output FITS file from each correlator thread is considered a ‘bank’ with a unique X-engine ID (XID; i.e., the correlator thread) ranging from 0 to 19 that is stored in the primary header of the FITS binary table.

The raw data output for both correlator modes are the covariance matrices

---

<sup>3</sup><https://github.com/GPU-correlators/xGPU/tree/master/src>

denoting the correlations of individual dipole elements. However, due to xGPU limitations, the covariance matrices are of size of  $64 \times 64$  (with elements for row and column over 40 being set to zero) and flattened to a one-dimensional data vector whose length depends on the specific correlator mode. An example of how the correlations are ordered is illustrated in Figure 4.1. Here,  $R_k^{ij}$  corresponds to the correlation between dipole  $i$  and  $j$  at frequency channel  $k$ . When in CALCORR mode, the bank file corresponding to XID ID 0 contains covariance matrices for frequency channels 0 to 4, 100 to 104, ..., 400 to 404; the XID 1 bank file stores covariance matrices for frequency channels, 5 to 9, 105 to 109, ..., 405 to 409. When in PFBCORR mode, the covariance matrices for channels 0 to 159 are stored in the bank file corresponding to XID 0 and continue in a linear and contiguous fashion such that the bank file corresponding to XID 19 stores data for frequency channels 3039 to 3199. The logic during data reduction is to process each frequency channel individually then sort the result into the final bandpass based on the XID and mode in which the data were taken. The methods employed to construct the two-dimensional form of the covariance matrices and sort the frequency channels are discussed in depth in Section 4.4.3.

## 4.4 The Data and Observations

Engineering and science commissioning observations were conducted over two separate observing runs in May and August of 2017 (GBT Project GBT16B.400). Calibration data obtained during the end of January 2017 as part of GBT projects

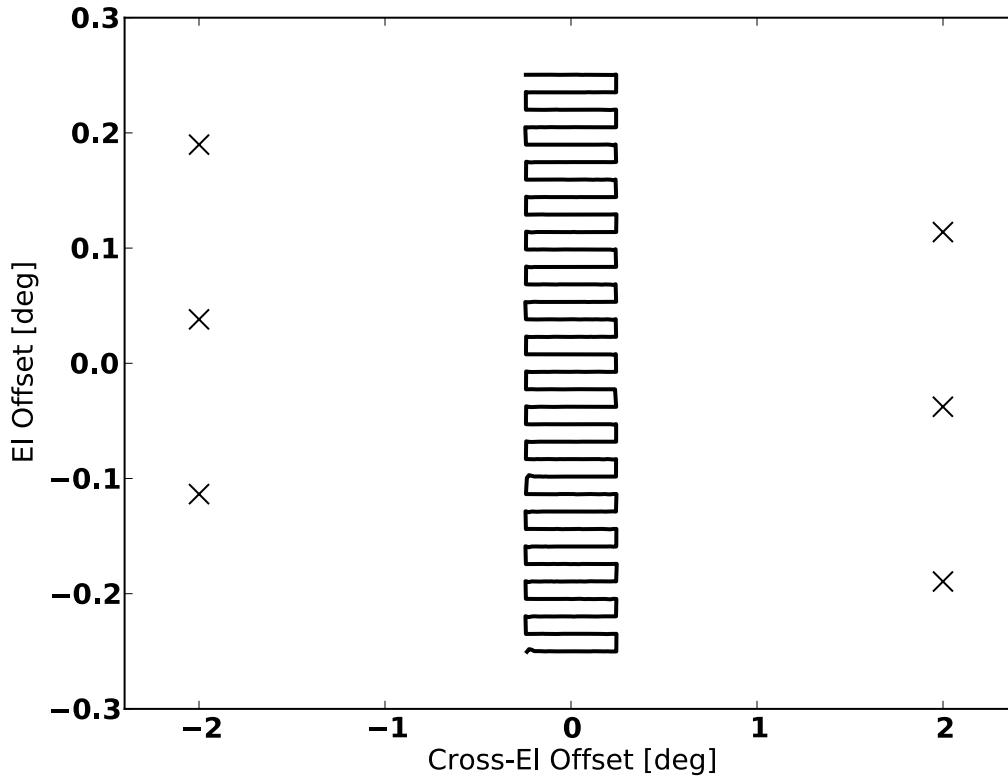


Figure 4.2 The trajectory of one of our calibration grids centered on 3C147. Off-pointings are denoted by the  $X$ , while the solid black lines represent the trajectory of the grid.

GBT17B\_360, GBT17B\_455 (mapping of the Galactic center), and GBT18A\_443 (mapping of a hydrogen recombination line region) are also included in the discussion regarding the quality of the beam former weights. The observations and backend setup covered in this work are summarized in Table 4.1.

#### 4.4.1 Calibration Observations

To obtain measurements of  $\mathbf{R}_s$  and  $\mathbf{R}_n$  with which to derive maxSNR weights, we employ two primary calibration scans. A ‘calibration grid’ involves moving the GBT in a grid centered on a strong calibrator spanning 30 arcminutes in cross-

Session	UT Date	UT Start	UT End	Schedule Block Type	Source	Mode	Integration Length [s]	LO [MHz]	Notes
<b>GBT16B_400_02</b>	2017-05-26	03:44:16	04:22:55	Calibration Grid	3C295	CALCORR	0.1	1450.00000	Continuous Trajectory
<b>GBT16B_400_03</b>	2017-05-27	04:17:55	05:12:11	Calibration Grid	3C295	CALCORR	0.1	1450.00000	Continuous Trajectory
<b>GBT16B_400_09</b>	2017-07-28	05:06:19	05:38:52	Calibration Grid	3C295	CALCORR	0.5	1450.00000	—
<b>GBT16B_400_12</b>	2017-08-04	04:16:54	05:03:33	Calibration Grid	3C295	CALCORR	0.5	1450.00000	40×40 □
	2017-08-04	05:30:27	06:02:27	DecLatMap	NGC6946	PFBCORR	0.5	1450.00000	41 columns
	2017-08-04	06:12:19	06:14:53	7Pt-Calibration	3C48	CALCORR	0.5	1450.00000	10 s Tracks
<b>GBT16B_400_13</b>	2017-08-04	13:44:40	14:29:09	Calibration Grid	3C123	CALCORR	0.5	1449.84841	—
	2017-08-04	14:42:46	15:14:47	DecLatMap	NGC6946	PFBCORR	0.5	1449.84841	41 columns
	2017-08-04	06:12:19	06:14:53	7Pt-Calibration	3C134	CALCORR	0.5	1449.84841	15 s Tracks
<b>GBT16B_400_13</b>	2017-08-06	15:54:43	15:59:43	OnOff	M31 Cloud 6	PFBCORR	0.5	1449.74271	five min ON scan
	2017-08-06	16:00:01	16:05:01	OnOff	M31 Cloud 6	PFBCORR	0.5	1449.74271	five min OFF scan
	2017-08-06	16:05:29	16:20:29	OnOff	M31 Cloud 6	PFBCORR	0.5	1449.74271	five min ON scan
	2017-08-06	16:10:37	16:15:37	OnOff	M31 Cloud 6	PFBCORR	0.5	1449.74271	five min OFF scan
	2017-08-06	16:15:55	16:20:55	OnOff	M31 Cloud 6	PFBCORR	0.5	1449.74271	five min ON scan
	2017-08-06	16:21:13	16:26:13	OnOff	M31 Cloud 6	PFBCORR	0.5	1449.74271	five min OFF scan
	2017-08-06	16:26:31	16:31:31	OnOff	M31 Cloud 6	PFBCORR	0.5	1449.74271	five min ON scan
	2017-08-06	16:31:39	16:36:39	OnOff	M31 Cloud 6	PFBCORR	0.5	1449.74271	five min OFF scan
	2017-08-06	16:41:15	16:43:58	7Pt-Calibration	3C147	CALCORR	0.5	1450.00000	15 s Tracks
	2017-08-06	16:44:48	17:22:16	Calibration Grid	3C147	CALCORR	0.5	1449.74271	—
<b>GBT17B_360_01</b>	2018-01-27	15:07:59	15:09:55	7Pt-Calibration	3C295	CALCORR	0.5	1450.00000	10 s Tracks
	2018-01-27	15:11:00	15:39:18	Calibration Grid	3C295	CALCORR	0.5	1450.00000	—
	2018-01-27	15:40:29	15:42:24	7Pt-Calibration	3C295	CALCORR	0.5	1450.00000	10 s Tracks
<b>GBT17B_360_02</b>	2018-01-27	18:32:59	18:36:07	7Pt-Calibration	3C295	CALCORR	0.5	1450.00000	10 s Tracks;
	2018-01-27	19:13:57	19:41:40	Calibration Grid	3C147	CALCORR	0.5	1450.00000	—
	2018-01-27	21:07:00	21:10:04	7Pt-Calibration	3C147	CALCORR	0.5	1450.00000	10 s Tracks
<b>GBT17B_360_03</b>	2018-01-28	06:44:29	06:47:38	7Pt-Calibration	3C295	CALCORR	0.5	1449.84841	10 s Tracks
	2018-01-28	06:48:56	07:17:23	Calibration Grid	3C295	CALCORR	0.5	1449.84841	—
	2018-01-28	08:05:49	08:36:44	DecLatMap	NGC4258 Field	PFBCORR	0.5	1449.84841	31 columns
	2018-01-28	08:05:49	08:36:44	DecLatMap	NGC4258 Field	PFBCORR	0.5	1449.84841	31 columns
	2018-01-28	08:38:28	09:07:35	DecLatMap	NGC4258 Field	PFBCORR	0.5	1449.84841	31 columns
<b>GBT17B_360_04</b>	2018-01-29	07:29:58	08:32:14	Calibration Grid	3C295	CALCORR	0.5	1450.00000	—
	2018-01-29	08:38:51	08:42:10	7Pt-Calibration	3C295	CALCORR	0.5	1450.00000	20 s Tracks
	2018-01-29	08:50:26	09:20:42	DecLatMap	NGC4258 Field	PFBCORR	0.5	1450.00000	31 columns
	2018-01-29	09:25:19	09:56:10	DecLatMap	NGC4258 Field	PFBCORR	0.5	1450.00000	31 columns
	2018-01-29	09:59:00	10:28:50	DecLatMap	NGC4258 Field	PFBCORR	0.5	1450.00000	31 columns
	2018-01-29	10:30:44	10:59:11	DecLatMap	NGC4258 Field	PFBCORR	0.5	1450.00000	31 columns
<b>GBT17B_360_05</b>	2018-01-30	12:02:53	12:13:08	7Pt-Calibration	3C295	CALCORR	0.5	1450.00000	20 s Tracks
	2018-01-30	12:18:09	12:50:55	DecLatMap	NGC4258 Field	PFBCORR	0.5	1450.00000	31 columns
	2018-01-30	12:53:24	13:00:44	7Pt-Calibration	3C295	CALCORR	0.5	1450.00000	20 s Tracks
<b>GBT17B_360_06</b>	2018-02-03	17:30:03	17:35:46	7Pt-Calibration	3C48	CALCORR	0.5	1075.00000	30 s Tracks
	2018-02-03	18:15:50	18:21:39	7Pt-Calibration	3C48	CALCORR	0.5	1250.00000	30 s Tracks
	2018-02-03	18:32:32	18:38:21	7Pt-Calibration	3C48	CALCORR	0.5	1350.00000	30 s Tracks
	2018-02-03	18:51:01	18:56:52	7Pt-Calibration	3C48	CALCORR	0.5	1550.00000	30 s Tracks
	2018-02-03	19:08:18	19:14:11	7Pt-Calibration	3C48	CALCORR	0.5	1650.00000	30 s Tracks
	2018-02-03	19:25:22	19:31:17	7Pt-Calibration	3C48	CALCORR	0.5	1750.00000	30 s Tracks
	2018-02-03	19:57:26	20:03:28	7Pt-Calibration	3C48	CALCORR	0.5	1449.74271	30 s Tracks
	2018-02-03	20:04:47	20:35:45	Calibration Grid	3C48	CALCORR	0.5	1449.74271	—
	2018-02-03	20:46:10	20:53:30	OnOff	M31 Cloud 6	PFBCORR	0.5	1449.74271	ON scan
	2018-02-03	20:53:30	—	OnOff	M31 Cloud 6	PFBCORR	0.5	1449.74271	OFF scan
<b>GBT17B_360_07</b>	2018-02-05	06:25:20	06:53:49	Calibration Grid	3C295	CALCORR	0.5	1450.00000	—
	2018-02-05	07:36:30	08:07:31	DecLatMap	NGC4258 Field	PFBCORR	0.5	1450.00000	31 columns
	2018-02-05	08:09:00	08:37:47	DecLatMap	NGC4258 Field	PFBCORR	0.5	1450.00000	31 columns
	2018-02-05	08:39:38	09:09:15	DecLatMap	NGC4258 Field	PFBCORR	0.5	1450.00000	31 columns
	2018-02-05	09:44:19	10:00:11	DecLatMap	NGC4258 Field	PFBCORR	0.5	1450.00000	columns 7 to 23
	2018-02-05	10:04:05	10:14:38	7Pt-Calibration	3C295	CALCORR	0.5	1450.00000	60 s Tracks

Table 4.1 Summary of FLAG Observations

Beam	GBT16B_400 Offset XEL [']	GBT16B_400 Offset EL [']	GBT17B_360 XEL Offset [']	GBT17B_360 EL Offset [']
0 (Boresight)	0	0	0	0
1	-4.55	7.88	-2.28	3.94
2	4.55	7.88	2.28	3.94
3	4.55	0	2.28	0
4	4.55	-7.88	2.28	-3.94
5	-4.55	-7.88	-2.28	-3.94
6	-4.55	0	-2.28	0

Table 4.2 Formed Beam Offsets

elevation (XEL) as set by the horizontal celestial coordinate system (i.e. ‘Encoder’ setting when using the GBT) and 34 rows spaced 0.91 arcminutes (approximately 1/10 the FWHM of the GBT beam at 1.4 GHz) apart in Elevation (EL). We compute  $\mathbf{R}_n$  by tracking two degrees in XEL away from the grid for a duration of ten seconds. We track after every fifth row to attain six total reference pointings with three evenly spaced on each side of the grid. To ensure adequate spatial sampling, we move the telescope at a rate of 0.91 arcminutes per second and dump integrations to disk every one second. The trajectory of the calibration grid observations performed during session 14 of GBT16B\_400 centered on 3C147 is shown in Figure 4.2 as the solid black lines, and the  $\mathbf{x}$  symbols representing the mean location of the reference pointings. Each integration within the grid can be paired with the closest reference pointing to derive an independent beam. The result is many independent beams over the entire 30 arcminute field of view (FOV) of the instrument that we can use to create a customized beam pattern. For both projects, we utilized a beam pattern that consisted of seven total beams arranged as a single boresight beam with the outer six beams placed as a symmetric hexagon. The offsets of each beam for each project is listed in Table 4.4.1. The compact offsets of GBT17B\_360 relative to those for GBT16B\_400 allows for the beam pattern to be exactly Nyquist sampled assuming a 9.1' FWHM for a single beam.

While it is interesting to obtain detailed spatial information of the array response provided by a calibration grid, the necessary  $\sim 30$  minutes of total observing time (including overhead) is disadvantageous. In the instances where beam offsets are explicitly chosen and seven total beams are desired, a seven point calibration

scan (or 7Pt-Cal), can be performed. This procedure involves (1) tracking the area of sky minus two degrees in XEL away from the source and at the same EL offset as the centers for beams five and six; (2) directly tracking the source (i.e. the boresight or zeroth beam); (3) slew the telescope such that the calibrator source is located at the desired center of beams one through six; (4) tracking the area of sky minus two degrees away from the source and at the same EL offsets as the centers of beams one and two. The two reference pointings at similar EL offsets as the outer beams allow for construction of  $\mathbf{R}_n$  (while also accounting for elevation-dependent effects), while the tracks on the desired beam centers collect the necessary response data to derive maxSNR weights. The duration of each track ranges between 10 and 30 seconds.

#### 4.4.2 Science Observations

The science data were collected using two distinct observing modes: (1) steering the telescope along columns of declination ( $\delta_{J2000}$ ) positioned at constant right ascension ( $\alpha_{J2000}$ ) coordinates to make on-the-fly maps and (2) position switching wherein the telescope first tracks the source, then tracks a reference position two degrees away in  $\alpha_{J2000}$ . These observing strategies were respectively executed using the available observing procedures of *DecLatMap* and *OnOff*.

The columns of  $\delta_{J2000}$  making up a *DecLatMap* are spaced every  $3'$  while dumping data every  $1.67'$  to ensure adequate spatial Nyquist sampling. For consistency with the calibration grid, the maps of NGC6946 were observed in Encoder (horizon-

tal coordinates) and extended two degrees in XEL and EL. There were a total of 41 scans in elevation. The maps of NGC6946 are centered on  $\alpha_{J2000}=20^h34^m52.3^s$ ,  $\delta_{J2000}=+60^\circ09'14''$ .

The *OnOff* observations were all performed on the faint HI source, M31 Cloud 6, which was first discovered by Wolfe et al. (2013). During the fourteenth session of project GBT16B\_400, each On-Off pair consisted of a five minute ON and five minute OFF scan to ensure equivalent noise properties. Note that the local oscillator is set to a specific topocentric frequency of 1449.74271 MHz in an attempt to center the source in a coarse channel. All spectral line observations were performed in the backend mode of PFBCORR to obtain a velocity resolution of 9.47 kHz ( $\sim 1.9$  km s<sup>-1</sup> in radial velocity).

### 4.4.3 Data Reduction

A given scan done with FLAG produces several types of ancillary FITS files written to `/home/gbtdata/PROJECT_SESSION` that contain important metadata such as the antenna positions. These metadata must be collated and combined with the raw correlations stored in the 20 bank FITS files to create a single dish FITS (SDFITS) file. This process is carried out by the `sdfits` program available on the GBO computing network. The unique format of the raw FLAG data necessitate custom software that not only collates all the metadata similar to `sdfits`, but also performs the post-correlation beamforming. This section summarizes the data reduction processes and pipeline for FLAG spectral line data.

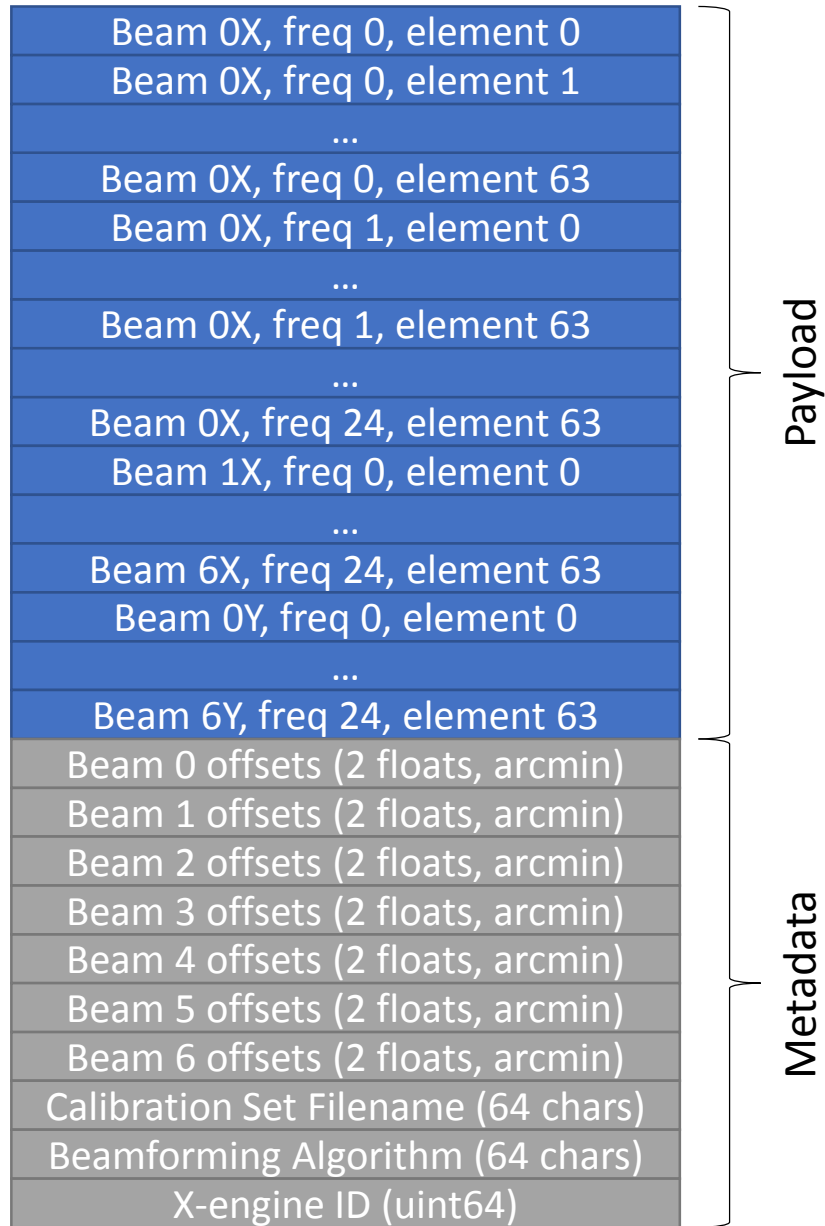


Figure 4.3 The structure of the binary files that contain the complex beamforming weights (Black 2018; private communication).

### 4.4.3.1 Processing Beamforming Weights

The first step in the filling process is to convert a set of 20 binary files (one for each bank) that stores the complex beamformer weights to FITS files to be accessed later to create the beamformed bandpasses. This is done with the script, `Weight_Filler.py`, that is a part of the `utils` available through the custom `SpectralFiller` Python package<sup>4</sup>. The primary purpose of this software suite is to generate a FITS file containing raw beamformed spectra in the units of counts. Figure 4.3 summarizes the format of these binary files. The first component of the file contains (in sequential order) the real and imaginary component of the complex weight for each polarization, beam, coarse frequency channel, and dipole element. Recall that the correlation matrices are of shape  $64 \times 64$ . Since we are only interested in the first 40 elements that correspond to the 40 available data ports ( $19 \times 2$  dipoles (dual polarizations) with two spare ports), the remaining elements are discarded. Once the FITS files that contain the weights are generated The ‘main’ script that creates an SDFITS file is `PAF_Filler.py`. This script processes each bank FITS file individually by reading in the associated weights and bank FITS files (identified through a common XID), computes Equation 4.8 for each frequency channel, and sorts the result into contiguous bandpass (recall that the data stored in the raw bank FITS files do not correspond to adjacent frequency channels). Aside from the post correlation beamforming, this script also collates all the necessary metadata and applies the beam offsets.

As of Spring 2018, the GBO LO and IF system managers cannot explicitly

---

<sup>4</sup><https://github.com/nipingel/SpectralFiller>

communicate with the new beamforming backend. In other words, this means the frequencies recorded for any observation are only recorded in the topocentric reference frame. However, since the RA/Dec values of each beam pointing center are available after the beam offsets are applied, a proper Doppler correction can be calculated. Currently the Doppler correction will be applied such that the IF frequencies will be in the Heliocentric reference frame with the OPTICAL velocity definition. Translations to other reference frames and velocity definitions (e.g., LSRK in the RADIO definition) can be performed in GBTIDL during further calibration. The code that performs the correction is an edited version of Frank Ghigo’s radial velocity correction calculator<sup>5</sup>. The final SDFITS file contains the raw beamformed spectra in units of ‘counts’ that can be manipulated within the GBTIDL environment exactly in the same manner as data from the VEGAS backend.

#### 4.4.4 Calibration and Imaging

Calibration begins by calculating the equivalent system flux density (SEFD) from the seven-point and grid scans. This quantity is the flux density equivalent of  $T_{\text{sys}}$ . The SEFD is convenient because it directly folds in the directly measurable  $T_{\text{sys}}/\eta$  ratio. Knowing the flux density of a source observed with a grid schedule block,  $S_{\text{CalSrc}}$  the system equivalent flux density is given by

$$S_{\text{SEFD}} = \frac{S_{\text{CalSrc}}}{\left(\frac{P_{\text{On}}}{P_{\text{Off}}} - 1\right)}, \quad (4.9)$$

---

<sup>5</sup><http://www.gb.nrao.edu/GBT/setups/radvelcalc.html>

where  $P_{\text{On}}$  and  $P_{\text{Off}}$  are respectively the On and Off power values. Two distributions of On and Off raw beamformed power values are built from the values generally contained between coarse channels corresponding to 1400.2 MHz to 1416.6 MHz and 1425.1 MHz to 1440.3 MHz to avoid Galactic HI emission and fit with separate Gaussian functions.  $P_{\text{On}}$  is taken to be the maximum value in the On distribution, while  $P_{\text{Off}}$  is taken as the fitted mean of the Off distribution. The respective uncertainties are the fitted rms given by the fit to the distinct distributions. All power values are corrected for atmospheric attenuation. The final uncertainty for the SEFD value is computed by propagating the statistical uncertainties of  $P_{\text{On}}$ ,  $P_{\text{Off}}$ , and  $S_{\text{CalSrc}}$ . The flux density of a given calibrator source is taken from Perley & Butler (2017). The flux density of a target source is then given by

$$S_{\text{src}} = S_{\text{SEFD}} \left( \frac{P_{\text{On}}}{P_{\text{Off}}} - 1 \right). \quad (1.10)$$

Similar to the calibration procedure outlined in Section 2.3.1, we obtain a reference spectrum to use as  $P_{\text{Off}}$  from the edges of our science maps by taking the mean power in each frequency channel for the first and last four integrations of a particular *DecLatMap* scan.  $P_{\text{On}}$  in Equation 1.10 is then the raw power in each integration recording during the *DecLatMap* procedure. The system equivalent flux densities used to scale the raw power ratios for each beam and each session are summarized in Table 1.4. The mean system equivalent flux density over all beams and the presented data is  $14.40 \pm 0.65$  Jy/beam. For the sake of direct comparison if we assume a gain of 1.86 K/Jy as derived in Section 2.3.1, this translates to a mean  $T_{\text{sys}}$  of about 27 K.

While this assumption does not consider specific parameters of the FLAG receiver, such as the the large spillover from the illumination pattern of individual dipoles and their mutual coupling, it is encouraging to see a very similar  $T_{\text{sys}}$  to that of the existing single pixel receiver ( $\sim 18$  K). The  $T_{\text{sys}}$  of FLAG and its overall sensitivity will be discussed further in Section 1.5.1.

An example of a raw and calibrated integration when the system is in PFB-CORR mode is shown in Figure 1.4. The nulls, or ‘scalping’, seen every 303.18 kHz (every 32 fine frequency channels) in the top plot is an artifact caused by the two stage PFB architecture approach currently implemented in the backend. As the raw complex time series data are processed within the ROACHs, a response filter is implemented in the coarse PFB such that the adjacent channels overlap at the 3 dB point to reduce spectral leakage. This underlying structure becomes readily apparent after the fine PFB implemented in the GPUs, however. The scalping therefore traces the structure of each coarse channel across the bandpass. While the structure is somewhat mitigated in the calibrated data (since there is a division by a reference spectrum), power variations caused by spectral leakage (power from adjacent channels) in the transition bands of the coarse channel bandpass filter result in residual structure. Additionally, this scheme leads to signal aliasing stemming from the overlap in coarse channels. This does not hinder the performance of FLAG in terms of sensitivity, but a fix for the signal aliasing is a top priority going forward. One suggested future scheme is to double the input coarse channel into the PFB such that the drop in power caused by the 3 dB overlap is avoided.

The scalping can be completely mitigated by dithering the frequency such

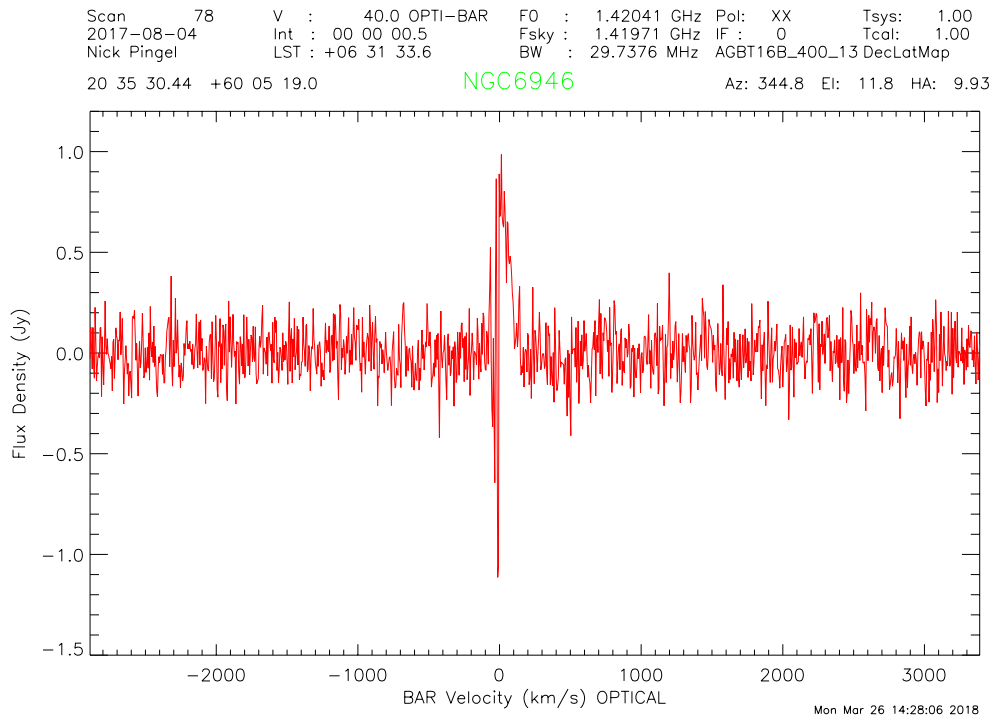
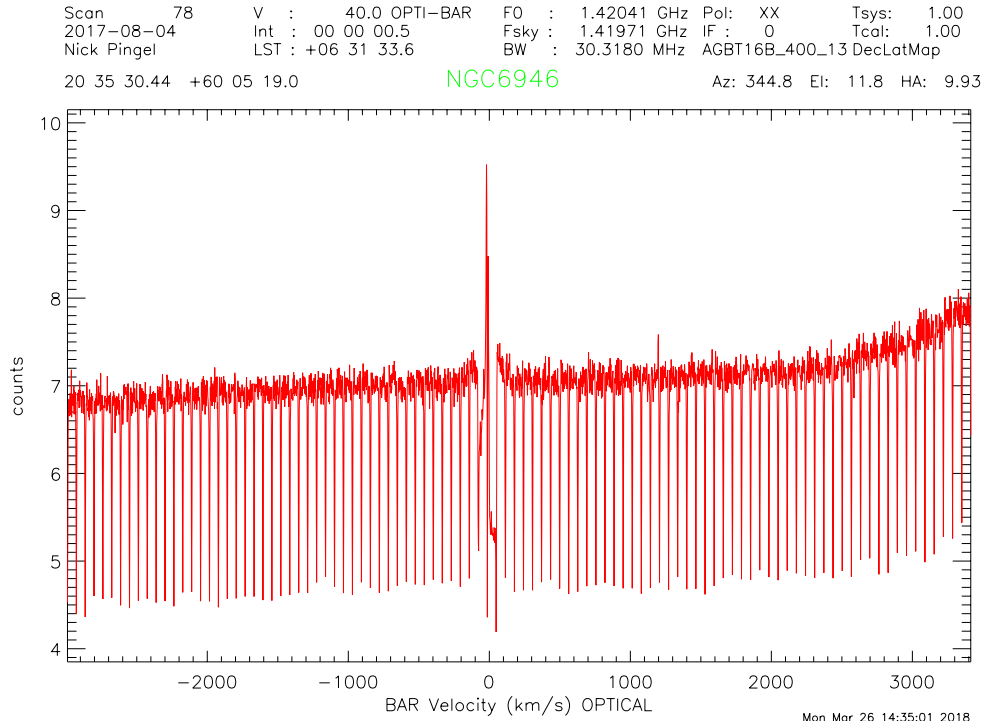


Figure 1.4 *Top*: An example of an uncalibrated, beamformed spectrum as seen in a GBTIDL plotter window taken from the 35th integration of the 19th column of a *DecLatMap* scan of NGC6946. The 3 dB drop in power (i.e., ‘scalloping’) is an artifact of the two step PFB implementation of the backend (see text). *Bottom*: The calibrated version of the above spectrum. While the scalloping behavior appears to be mitigated, the signal aliasing at the edge of a coarse channel is still present.

that a subsequent map has a central frequency that is either 151.59 kHz (or one-half of a coarse channel width) above or below the initial LO setting. In the case of NGC6946, the LO was shifted by  $-151.59$  kHz to be at 1449.84841 MHz. Before the integrations from a science observation are correctly scaled to units of Jy, the six fine frequency channels that span adjacent coarse channel edges and are thus affected by the scalloping are blanked. The exact shift necessary to fill in the blanked regions is computed and applied to the spectra with the higher LO setting. The final flux value in a given frequency channel is the weighted average of the original fluxes from the individual low and high frequency dithered mapping scans, where the weights are nominally the inverse squared equivalent system flux densities. It is somewhat common for a correlator thread to terminate (or drop out) due to issues with the data throughput, which ultimately leads to blank discontinuities in the spectra that span the width of a coarse channel, or 303.18 kHz and blank flux values. If a flux value from any of the contributing frequency dithered spectra are blank due to a drop out, a weight of 0 is adopted. The final weighted spectra are then smoothed to a velocity resolution of  $5.2 \text{ km s}^{-1}$  (24.414 kHz). The data from separate beams are combined using the AIPS task DBCON and imaged using a convolution function of a Gaussian-tapered circular Bessel function available in the task SDGRD. Note that due to problems with dead dipole elements, only weights for the XX polarization are used in the beamforming of the science observations presented in this chapter, but the behavior of the YY polarization is still analyzed for the calibration data.

## 1.5 Results

The important aspects of the spectral line modes of FLAG to explore with the science observations outlined above are:

- How the  $T_{\text{sys}}$  (or  $S_{\text{SEFD}}$ ) of individual beams behave over time?
- How well these values compare with the single pixel receiver
- How does the noise behave with what is expected theoretically?
- In turn, what is the overall increase in the survey speeds?
- How do the FLAG maps compare to maps made with the single pixel receiver in terms of spatial coincidence of emission, total flux, and detection of low column density features?

### 1.5.1 $T_{\text{sys}}$ and Noise Properties

By observing some reference position in addition to an ‘On source’ scan, the theoretical signal-to-noise ratio (S/N) is given by

$$\frac{T_{\text{a}}}{\sigma}, \quad (1.11)$$

where  $T_{\text{a}}$  is the antenna temperature for the On source observation and  $\sigma$  is the theoretical rms noise determined by the ideal radiometer equation

$$\sigma = \frac{T_{\text{sys}}}{\sqrt{N_{\text{pol}}\Delta\nu t_{\text{eff}}}}, \quad (1.12)$$

where  $N_{\text{pol}}$  is the number of polarizations,  $\Delta\nu$  represents the frequency width of an individual channel, and  $t_{\text{eff}}$  is the effective integration time (Condon & Ransom, 2016).  $T_a$  in the above equation is related to the intensity of incident radiation through the blackbody equation in the Rayleigh-Jeans limit

$$I_{\text{src}} = \frac{2kT_a}{\lambda}. \quad (1.13)$$

The total power  $P_{\text{src}}$  incident (from an unpolarized source) at some wavelength  $\lambda$  on an antenna is the  $I_{\text{src}}$  detected over some infinitesimal, physical area  $dA$  measured over the solid angle of the source,  $d\Omega$ , in steradians

$$P_{\text{src}} = I_{\text{src}} dA d\Omega = \left( \frac{2kT_a}{\lambda^2} \right) (dA d\Omega). \quad (1.14)$$

Knowing that that  $(dA d\Omega) = \lambda^2$  from the Antenna Theorem (Condon & Ransom, 2016), the expression for the source power received by the telescope is then

$$P_{\text{src}} = 2kT_a. \quad (1.15)$$

Substituting this result into the left-hand side and integrating up to the average effective area  $A_e$  that measures the total area of the primary reflector illuminated by the feed and beamsize  $\Omega_B$  reduces Equation 1.14 to

$$2kT_a = I_{\text{src}} A_e \Omega_B. \quad (1.16)$$

Finally, knowing that the flux is  $I_{src}$  over the beam  $\Omega_B$ , and putting  $A_e$  in terms of the aperture efficiency,  $\eta$ , which is essentially a measure of how well a particular feed illuminates the collecting surface, the geometric area  $A_g$ , an expression for the  $T_a$  can be obtained such that

$$T_a = \frac{S_{src} A_g \eta}{2k}. \quad (1.17)$$

If ideal observations of blank sky are being recorded, the measured  $T_a$  is approximately equal to  $T_{sys}$  and Equation 1.17 becomes

$$\frac{T_{sys}}{\eta} = \frac{S_{SEFD} A_g}{2k}. \quad (1.18)$$

Substituting the definition for  $S_{SEFD}$  in from Equation 4.9 and putting the power levels in terms of the product between correlation matrices and beamforming weights from Equation 4.8 results in the expression

$$\frac{T_{sys}}{\eta} = \frac{S_{CalSrc} A_g}{2k} \frac{\mathbf{w}^H \mathbf{R}_n \mathbf{w}}{\mathbf{w}^H \mathbf{R}_s \mathbf{w}}. \quad (1.19)$$

This equation is an oft-used metric to compare the performance of different PAFs (Jeffs et al., 2008; Landon et al., 2010; Roshi et al., 2018) as it can be directly measured. Since each electronically formed beam has a unique  $S_{SEFD}$ , a  $T_{sys}/\eta$  value can be also be measured for each beam.

Figure 1.5 shows how  $T_{sys}/\eta$  typically varies across the bandpass for a single beam (in this case the boresight beam). A characteristic value is computed by taking the mean between frequencies of 1400.2 to 1416.6 MHz and 1425.1 to 1440.3

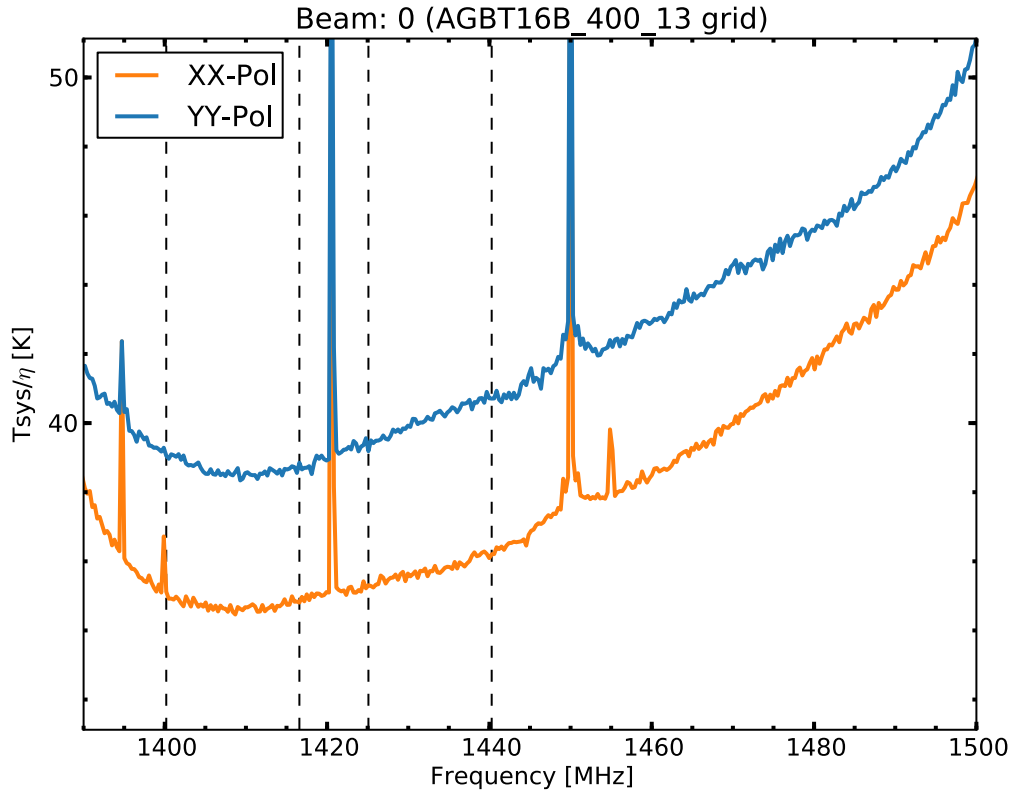


Figure 1.5  $T_{\text{sys}}/\eta$  for the boresight beam from a grid calibration observation of 3C295 from 16B\_400\_13. The vertical dashed lines enclose the frequencies over which the mean value was computed. Note that the Galactic HI frequencies are excluded from this calculation. The spike at 1450 MHz is due to the DC component of the Fourier Transform of the complex time series data.

Beam	Mean $T_{\text{sys}}/\eta$ (XX) [K]	Mean $T_{\text{sys}}/\eta$ (YY) [K]	Mean $S_{\text{sys}}$ [Jy/beam] (XX)
0 (Boresight)	35.70±0.49	44.91±0.97	12±1
1	34.70±0.49	39.51±0.97	13±1
2	34.90±0.58	46±2	12±1
3	35.04±0.80	53±1	14±2
4	39.77±0.71	52±2	14±2
5	36.02±0.60	44.31±0.76	14±2
6	37.72±0.71	41.44±0.64	14±2

Table 1.3 Mean  $T_{\text{sys}}/\eta$  over all sessions

MHz. Again, two distinct frequencies ranges are used to avoid Galactic HI emission near the 1420.4 MHz. In principle, each raw count value used to beamformed power ratio in Equation 1.19 value for a discrete frequency channel bin will have an associated error similar to the SEFD; however, as these were not readily available the associated uncertainties for the quoted  $T_{\text{sys}}/\eta$  in this dissertation are purely the statistical uncertainties from computing the characteristic value. The increase of  $T_{\text{sys}}/\eta$  towards the edge of the bandpass is due to the roll-off in the analog filter where gain will decrease (in turn causing an increase in  $T_{\text{sys}}$ , while the large spike at 1450 MHz is due to the DC component of the Fourier Transform of the raw complex time series data.

Two major aspects regarding the overall performance of FLAG are how  $T_{\text{sys}}/\eta$  for each distinct beam changes as function of time and the length of time the complex beamforming weights stay valid. Figure 1.6 shows the temporal variation of  $T_{\text{sys}}/\eta$  for the boresight beam. The points are taken from all available calibration data over all sessions. The abscissa values of duration are computed by taking the mean decimal modified Julian date (DMJD) during a given calibration scan. The reference DMJD is taken to be the first calibration scan of the respective observing run.

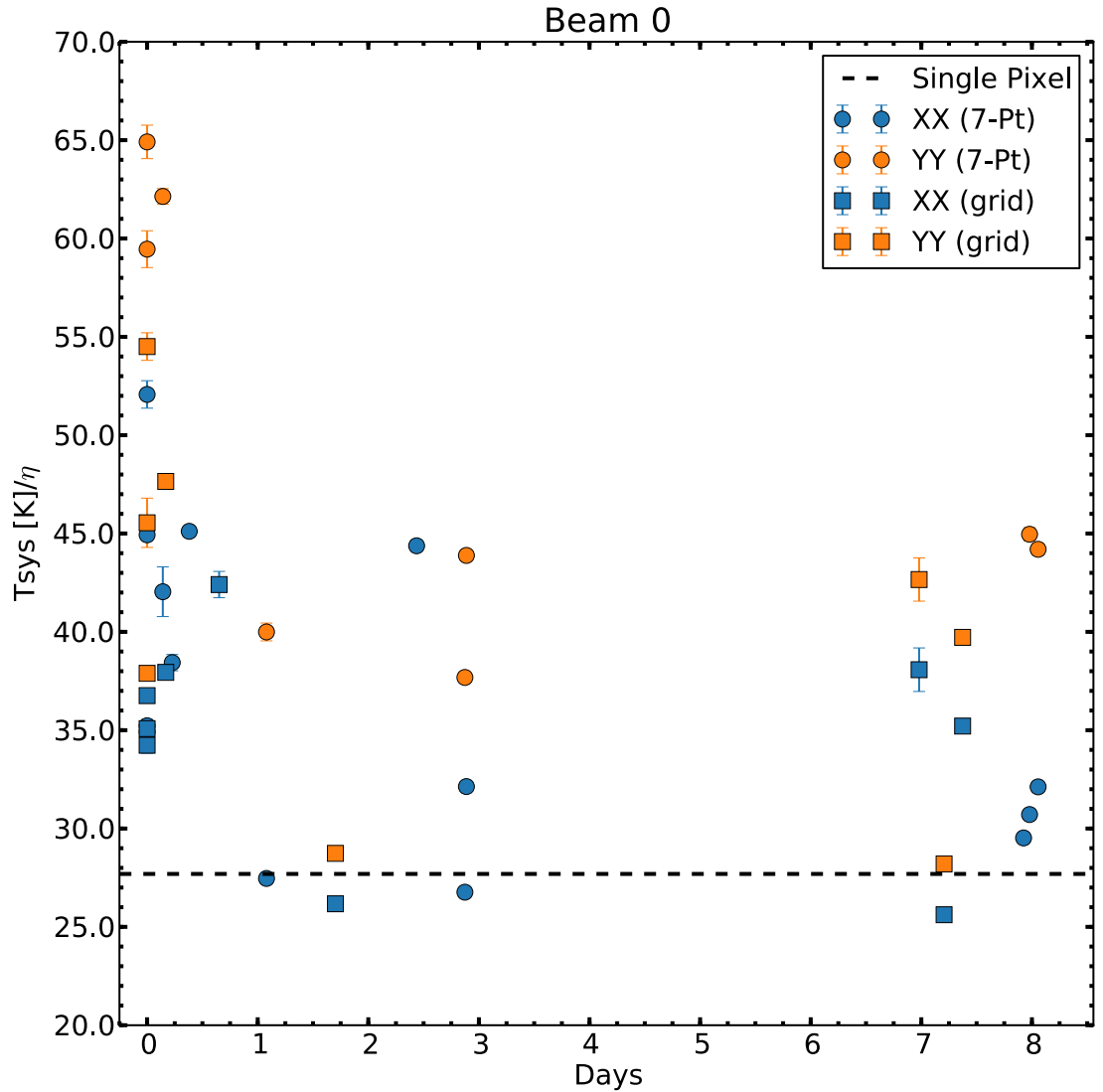


Figure 1.6 Temporal variation of  $T_{\text{sys}}/\eta$  for the boresight beam. The circle points denote values derived from a seven-point calibration, while the square points are computed from grid calibrations. The general trend of high values for the YY polarization, while the XX polarization is relatively stable over the duration of a given observing run, is true for all outer beams. The calibration data shown here is taken from all observing runs. The horizontal dashed line represents the value estimated for the existing single-pixel feed.

Session	Beam	Scan Type	$T_{\text{sys}}/\eta$ [K]	$S_{\text{sys}}$ [Jy/beam]	Calibration Source	Source Flux [Jy]
<b>GBT16B.400.12</b>						
	0	Grid	36.75±0.17	13±1	3C295	22.15
	1	Grid	44.00±0.13	15±2	3C295	22.15
	2	Grid	41.92±0.12	14±2	3C295	22.15
	3	Grid	43.52±0.13	15±1	3C295	22.15
	4	Grid	44.70±0.13	16±2	3C295	22.15
	5	Grid	47.91±0.13	16±2	3C295	22.15
	6	Grid	49.18±0.17	16±2	3C295	22.15
<b>GBT16B.400.13</b>						
	0	Grid	35.22±0.22	11±1	3C295	22.15
	1	Grid	36.53±0.23	12±3	3C295	22.15
	2	Grid	39.52±0.20	12±1	3C295	22.15
	3	Grid	37.52±0.33	13±1	3C295	22.15
	4	Grid	39.08±0.13	13±1	3C295	22.15
	5	Grid	39.60±0.17	13±1	3C295	22.15
	6	Grid	38.27±0.18	13±1	3C295	22.15
<b>GBT16B.400.14</b>						
	0	Grid	37.50±0.33	11±1	3C147	21.25
	1	Grid	36.67±0.25	12±1	3C147	21.25
	2	Grid	39.52±0.20	11±1	3C147	21.25
	3	Grid	40.85±0.22	13±1	3C147	21.25
	4	Grid	39.35±0.18	14±2	3C147	21.25
	5	Grid	47.05±0.85	13±1	3C147	21.25
	6	Grid	44.22±0.47	12±1	3C147	21.25

Table 1.4 Summary of derived system properties in XX Polarization from calibration scans used to make the science images

The  $T_{\text{sys}}/\eta$  for the XX polarization in the boresight beam has relatively little scatter around the mean of  $35.7\pm 0.8$  K, while the YY polarization values are consistently higher with a mean value of  $40\pm 1$  K with the highest values coming at the beginning of observing runs. The increase towards higher and lower frequencies is the effect of hitting the analog filter roll-off, resulting in the overall shape of a second order polynomial. The slight increase in YY values are due to several factors such as known dead LNAs, a more favorable backend setup (the first few sessions only ran with a single HPC), calibration grids that include more (and evenly spaced) reference scans (calibration grids for GBT16B.400.1 to GBT16B.400.9 only included two reference scans), and/or better bit and byte lock. The trends for  $T_{\text{sys}}/\eta$  presented in this plot is representative for the outer beams. The time averaged  $T_{\text{sys}}/\eta$

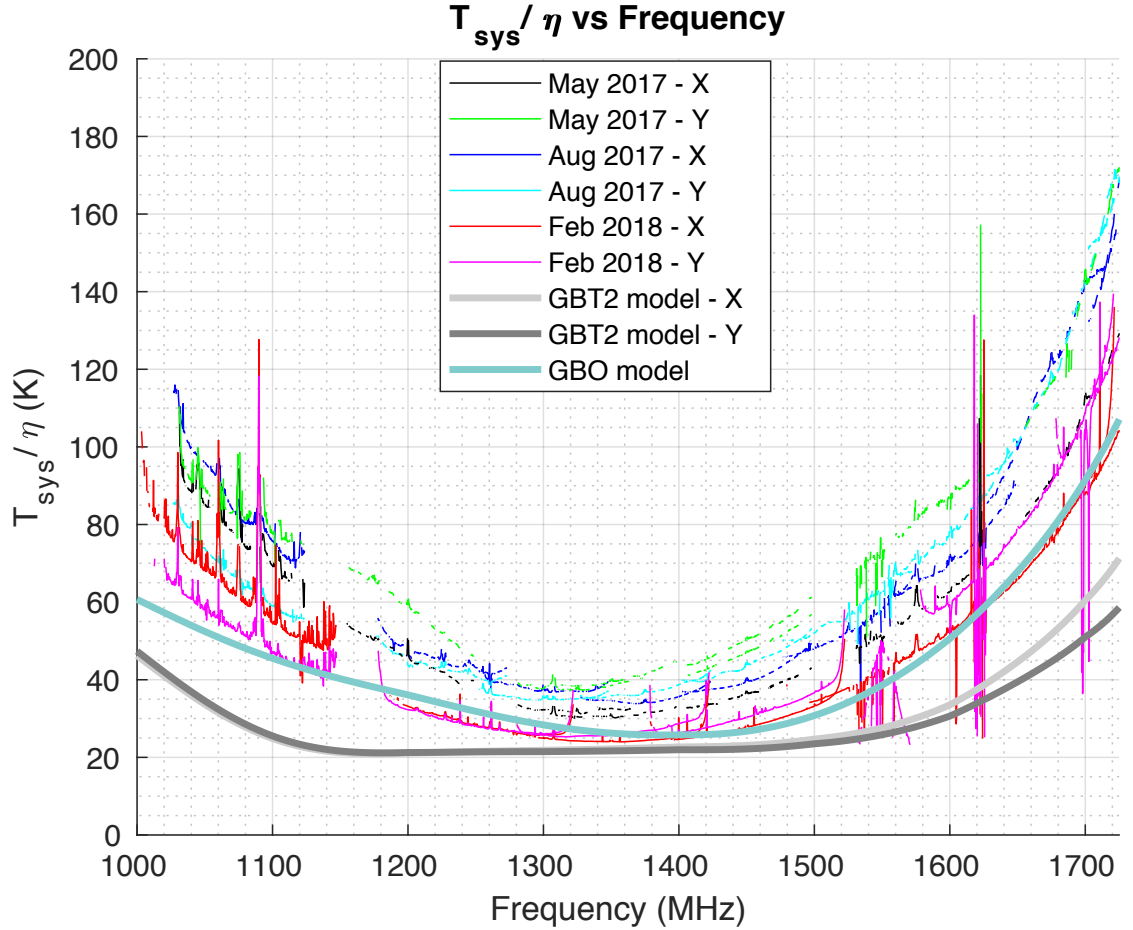


Figure 1.7 Temporal variation of  $T_{\text{sys}}/\eta$  for the boresight beam over the entire analog frequency range. The general trend of decreasing  $T_{\text{sys}}/\eta$  is also true for all outer beams.

for each beam and polarization are shown in Table 1.3.

The dashed black line horizontal line at 27.7 K represents the  $T_{\text{sys}}/\eta$  of the existing L-Band receiver on the GBT, assuming a  $T_{\text{sys}}$  value of 18 K and  $\eta = 0.65$  (Boothroyd et al., 2011). While most of the  $T_{\text{sys}}/\eta$  lie above this benchmark for the boresight beam, several seven-point and grid calibration observations are at or exceed single pixel performance. Again, this behavior is also true for the outer beams.

Figure 1.7 shows the decrease in  $T_{\text{sys}}/\eta$  derived from ‘frequency sweep’ observa-

tions of a calibration source. The observing procedure was to perform a seven-point calibration scan with the LO set to 50 MHz increments beginning at 1100 MHz and continuing up to 1700 MHz, measure the  $T_{\text{sys}}/\eta$  quantity as a function of the 150 MHz bandpass for each formed beam, and merge the results. There is a trend of decreasing  $T_{\text{sys}}/\eta$  as a function of time for both polarizations with the February 2018 calibration data showing the lowest observed  $T_{\text{sys}}/\eta$ , which can be attributed to improvements made to the signal processing algorithms of the backend. Specifically, a bit underflow when the data in the ROACH is reduced to 8-bit/8-bit real and imaginary values just before packetization.

A correction to increase the digital gain just prior to the re-quantization was implemented for the August 2017 and February 2018 observing runs. For some frequencies, namely 1200 MHz to 1400 MHz, the derived  $T_{\text{sys}}/\eta$  even out performs the GBO model in Figure 1.7. While this figure again only shows data for the boresight beam, the trend is observed in all outer beams.

A figure of merit to compare the performance of FLAG to the existing single-pixel feed is the respective noise from a single *DecLatMap* procedure. As discussed in Section 4.4.1, a typical science map is 4 deg<sup>2</sup> centered on the source and consists of 41 total columns that span 2° made up of 71 distinct integrations dumped every 1.67'. Consider an integration time of the single-pixel map ( $t_{\text{int},SP}$ ) set at 5 s as compared to 0.5 s for an default FLAG observation. Thus, the rate at which the telescope moves is 0.33 arcminutes s<sup>-1</sup> and 3.33 arcminutes s<sup>-1</sup> for a single-pixel and FLAG map, respectively. The area of the single-pixel GBT beam with a full-width half-max (FWHM) of 9.1' is  $1.1331 \times \text{FWHM}^2 \sim 94$  arcminutes<sup>2</sup>. A standard

*DecLatMap* will therefore have  $\sim 154$  GBT beams. Excluding overhead, a single pixel map takes a total of  $t_{map,SP} = 71 \times 41 \times t_{int,sp} = 14555.0 \text{ s} = 4.04 \text{ hours}$ , while an equivalent FLAG map takes  $t_{map,FLAG} = 1455.5 \text{ s} = 0.404 \text{ hours}$ . Dividing the total time for the two maps by the number of beams gives a total ‘signal’ integration time ( $t_{sig}$ ) of 95.1 s/beam and 9.5 s/beam for the single-pixel and FLAG, respectively. Recall that spectral line mapping data are calibrated by using the first and last four integrations of particular scan. The effective integration time for the single pixel map is then

$$t_{\text{eff}} = \frac{t_{\text{sig}} t_{\text{ref}}}{t_{\text{sig}} + t_{\text{ref}}} = \frac{95.1 \cdot 40}{95.1 + 40} = 28.2 \text{ s/beam.} \quad (1.20)$$

Repeating the calculation for the equivalent FLAG map gives 2.8 s/beam. The factor of 10 decrease is due to  $t_{\text{int},FLAG}$  being set to 0.5 s as opposed to 5 s; thus,  $t_{\text{map},FLAG}$ ,  $t_{\text{ref}}$ , and  $t_{\text{sig}}$  are similarly a factor of 10 lower. This is *not* to say that a single equivalent FLAG map will reach the same sensitivity in  $10\times$  less time.

The predicted root-mean-square (rms;  $\sigma$ ) is given by the ideal radiometer equation in Equation 1.12. Recall that only the XX polarization is analyzed, so  $N_{pol}$  is equal to one),  $\Delta\nu$  represents the frequency width of a single velocity channel (typically 24.414 kHz). In our case, the equivalent system flux density derived from Equation 4.9 can be directly substituted for  $T_{\text{sys}}$  in the equation above to calculate the theoretical rms noise in units of Jy/beam. Utilizing the antenna of gain of 1.86 K/Jy derived in Section 2.3.1 and assuming a  $T_{\text{sys}}$  of 18 K, the equivalent  $S_{\text{SEFD}}$  for a typical single pixel observation is 9.68 Jy/beam. Plugging in the respective  $t_{\text{eff}}$  values for a typical the single-pixel and FLAG map, and taking the mean  $S_{\text{SEFD}}$

of the boresight beam used to scale all science observations in Table 1.4, gives the theoretical rms respectively as 12 mJy/beam versus 36 mJy/beam for a single polarization in the single pixel and single formed beam in the FLAG maps, respectively. Assuming 36 mJy/beam for the other six electronically formed beams in a FLAG map, the predicted FLAG noise should drop by a factor of  $1/\sqrt{7}$  to be 13.6 mJy/beam, which compares reasonably well to an equivalent single-pixel map. There is, of course, inherent scatter in  $S_{\text{SEFD}}$ . A more exact calculation for the noise in a single FLAG map is

$$\sigma = \frac{1}{\sqrt{N \cdot N_{\text{pol}} \Delta\nu t_{\text{eff}}}} \sum_{i=1}^N S_{\text{SEFD},i}, \quad (1.21)$$

where  $N$  is the total number of beams (usually seven, in our case). Plugging in the mean  $S_{\text{SEFD}}$  for each beam as shown in Table 1.4 and again considering only a single polarization, the typical rms noise for a typical FLAG map will be 55 mJy/beam. Scaling the  $t_{\text{eff}}$  of 2.82 s/beam for a single electronically formed FLAG beam by a factor of 7 to account for all formed beams, and taking the ratio of the result with the single-pixel  $t_{\text{eff}}$  of 28.20 s/beam gives 1.4. This ratio implies an observer can reach an equivalent  $t_{\text{eff}}$  in  $1.4 \times t_{\text{map,FLAG}}$ , or 0.57 hours. Thus, the total mapping time required to reach an equivalent single pixel  $t_{\text{eff}}$  reduces by a factor of  $t_{\text{map,SP}}/0.57 = 4.04/0.57 \sim 7$ .

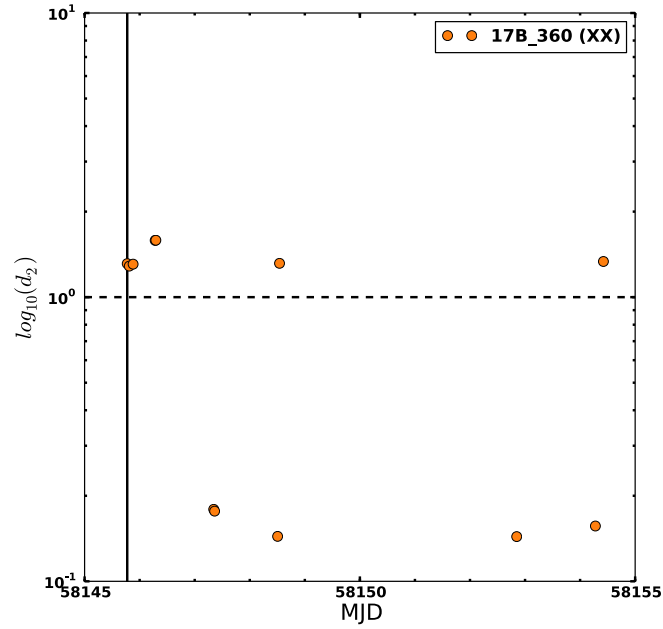
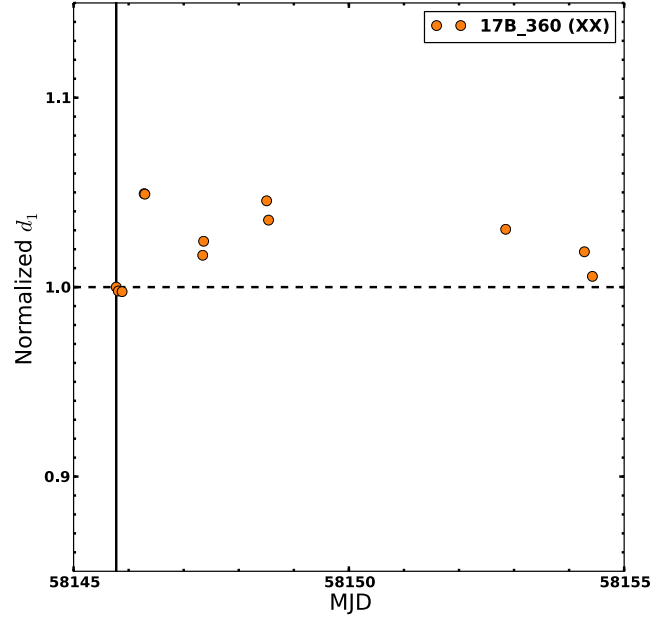


Figure 1.8 Normalized  $d_1$  (see text; top) and  $d_2$  (bottom) between the first and subsequent weight calibration vectors for GBT17B.360 sessions 01 to 07, GBT17B.455 session 01, and GBT18A.443 session 01 (orange). All values shown are for the boresight beam in XX polarization, though very similar trends exist for the outer beams. The horizontal dashed lines show where these quantities would indicate perfect agreement over time, while the solid vertical line denotes the beginning MJD of the observing run.

## 1.5.2 Beamformer Weight Validity over Time

The calibration procedures described above, while straightforward and not too time consuming, still contribute to about 30 minutes of overhead and, in principle, are only valid for a given ‘word/bit lock’. The front end employs a new digital-down-link mechanism that performs all analog-to-digital conversions in a compact assembly that sits at prime focus (Morgan et al., 2013). Two integral processes in the success of the DDL are achieving word and bit lock, which respectively refer to the recovery of the most-significant bit from each input sample and the deserialization bit alignment along the optical fiber. Since word/bit lock is currently lost with every change in the LO setting, an observer must derive fresh beam weights at the beginning of each observing session to achieve any formed beams on the sky and maintain an advantage over a traditional single pixel feed. Other reasons recalibration may be necessary include large variations in the contribution of spillover and sky noise to the signal model and the relative electronic gain drift between dipoles (Jeffs et al., 2008). Important factors that impact the quality of the weights include robust word and bit locks, constraining the desired steering vector for a formed beam, and utilizing a sufficiently bright calibration source to adequately characterize the system response when on and off source.

While the current state of the FLAG system requires new beamforming weights every session, it is still interesting to explore how the complex weight vectors derived from a given calibration observation vary with time between sessions and even different calibration scans within the same session. Studying the variations will help

reveal characteristic properties and/or behavior of the weights that demonstrate the stability of the system with time.

Recall that an element in the weight vector as described by Equation 4.2 is a complex number that contains the amplitude and phase information to be applied to the output of a given dipole in order to steer a beam in a given direction. It is therefore sensible to compare these two quantities to obtain a qualitative description of these weights over time. Dramatic variations in the phase indicate that the two weight vectors being compared will not provide reliably similar on-sky beam patterns, since the directional response to an incoming signal originating from the same incidence angle will be different. To measure the difference in phase, a distance metric can be defined

$$d_1 = \|\mathbf{a}_1 - \tilde{\mathbf{a}}_2\|, \quad (1.22)$$

where  $\mathbf{a}_1$  and  $\mathbf{a}_2$  are the vector norms (i.e., the square root of the sum of each element's squared complex modulus) of the weight vectors, or  $\mathbf{w}_1/\|\mathbf{w}_1\|$  and  $\mathbf{w}_2/\|\mathbf{w}_2\|$ , respectively.

The vector  $\tilde{\mathbf{a}}_2$  represents the subsequent weight vector that has been corrected for the 'bulk phase difference' between the two vectors. This bulk phase offset arises from the steering vectors, which are found by solving for the dominant eigenvector in the generalized eigenvalue problem in Equation 4.7. Since eigenvectors are basis vectors that have arbitrary scaling, it is the unknown scaling of the phase between calibration data sets that contributes to the bulk phase offset. A subsequent weight vector can be phase aligned to some initial weight vector by first making the first

element of  $\mathbf{a}_1$  real and then computing

$$\hat{\phi} = \angle(\mathbf{a}_2^H \mathbf{a}_1), \quad (1.23)$$

where  $\hat{\phi}$  is the angle of the Hermitian product of  $\mathbf{a}_2^H \mathbf{a}_1$ . The phase aligned weight vector is therefore  $\tilde{\mathbf{a}}_2 = e^{i\hat{\phi}} \mathbf{a}_2$ .

Because the distance metric  $d_1$  is the overall magnitude of an element-wise difference between two  $M$  element vectors, it encapsulates all the phase differences between respective dipoles into a single quantity. Small variations in  $d_1$  over time indicate similar phases (save for the bulk phase offset due, in part, to new word/bit lock) between the derived weight vectors, meaning the direction response of the array is stable over time; thus, the beam pattern shape and  $T_{\text{sys}}/\eta$  remain relatively unchanged.

The two vectors used to compute  $d_1$  are unit normalized, so it does not describe the scale variations between two weight vectors. Large variations in the relative scale will affect the gain stability over the field-of-view, and may cause difficulties in flux calibrations between observing sessions. To detail this behavior a separate distance metric can be defined

$$d_2 = \|\mathbf{w}_2\|/\|\mathbf{w}_1\|. \quad (1.24)$$

Figure 1.8 shows the  $d_1$  (top) and  $d_2$  (bottom) as a function of time for the 16B\_400 run consisting of sessions 09 to 14 (blue) and 17B\_360 run consisting of sessions 01 to 07 (blue) and calibration data from 17B\_455\_01 (orange) and 18A\_443\_01

(orange). Note that  $d_1$  is normalized to the value computed between the first weight vector derived for a particular observing run and the subsequent weight vector from the next calibration observation to represent a fractional change. A value of unity for both quantities indicates no variation in the weight vectors over time. Only mild variation ( $\lesssim 5\%$ ) is seen in the distance metrics tracing the total change in phase over time, indicating that the directional response to identical coincident signals is very similar over time. However, the same cannot be concluded for the scale variations as traced by  $d_2$ . For several sessions in the 17B\_360 the amplitude fluctuates between factors of 20 to 40, although the weight vectors derived for 16B\_400 are relatively stable. While not affecting overall sensitivity, such large amplitude variations introduce significant difficulties in the process of matching flux scales between observations. This is especially arduous when multiple observing sessions of the same object are needed to be combined. If such behavior can be determined during an observing session, it would be prudent of the observer to consider re-deriving the weight vector to acquire a more consistent amplitude.

### 1.5.3 HI FLAG Observations

Two key milestones for the FLAG system are the detection of HI in an extragalactic source and the complete recovery of the HI emission as already traced by the single pixel feed. This subsection will therefore focus on the results of observations of two sources that have ample existing GBT data for comparisons of the noise, spatial and spectral coincidence, and overall flux scaling.

### 1.5.3.1 NGC6946

The HI distribution in NGC6946 is well studied utilizing both high angular resolution VLA data (Boomsma et al., 2008) and GBT data. This particular source is an ideal candidate for testing the sensitivity of the FLAG maps given the single pixel GBT data for NGC6946 with an rms noise of 8 mK per  $5.2 \text{ km s}^{-1}$  velocity channel, or a  $3\sigma$   $N_{\text{HI}}$  detection level of  $4.5 \times 10^{18} \text{ cm}^{-2}$  over a  $20 \text{ km s}^{-1}$  spectral line, and the presence of several companion galaxies in the field (Pisano, 2014). Furthermore, the proximity of the source emission in relation to Milky Way emission and the relatively large angular extent of the emission in and around NGC6946 provide good tests for spatial and spectral coincidence in the beam-combined data (see procedure described in Section 4.4.4).

Figure 1.9 shows the flux as a function of velocity for the single pixel data (orange line) and FLAG data (blue). Each FLAG data cube was regridded to the same FOV and spectral scale as the single pixel data cube to ensure the flux was measured over the exact same angular area. For all instances save for Beam 3, we see that the flux as detected by FLAG is  $\sim 30\%$  lower than what is detected by the single pixel data.

There could be several reasons for such a large flux offset between the two data sets. A particularly conspicuous source for the offset may also lie in the weighted average of the two frequency dithered bandpasses. The flux as a function velocity is again plotted but for the cubes generated from GBT16B\_400\_12 (LO at 1450.0000 MHz) and GBT16B\_400\_13 (LO at 1449.8484) MHz in Figures 1.10 and 1.11, re-

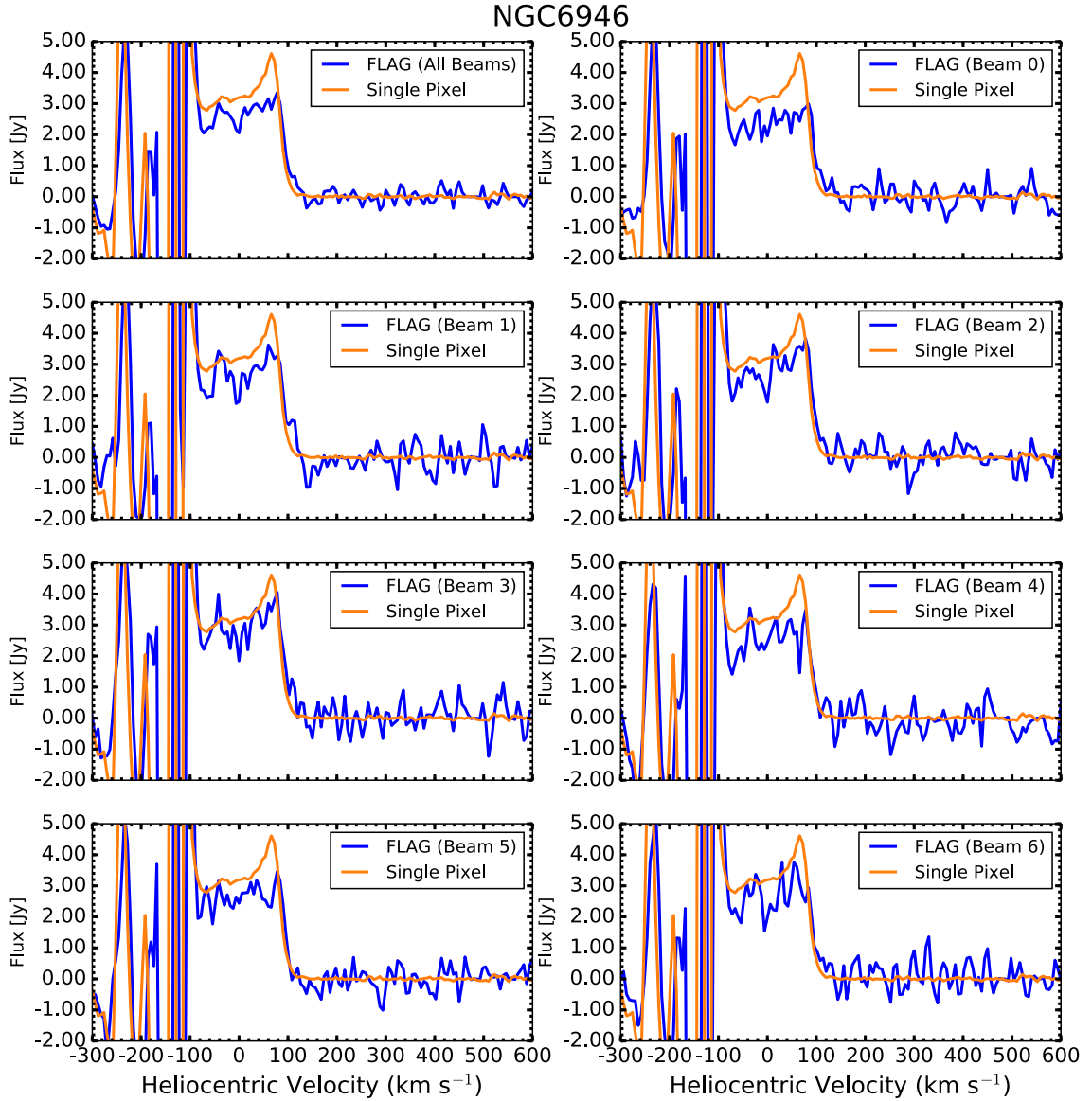


Figure 1.9 HI profiles showing flux as a function of velocity for the combined data set (all beams; top left), in addition to the seven individual beams. All data are from the weighted average combination of the frequency dithered observations from sessions GBT16B\_400\_12 (LO set to 1450.00 MHz) and GBT16B\_400\_13 (LO shifted down one-half of a course channel to 1449.85 MHz). The data are weighted by the respective  $S_{SEFD}$  for each beam.

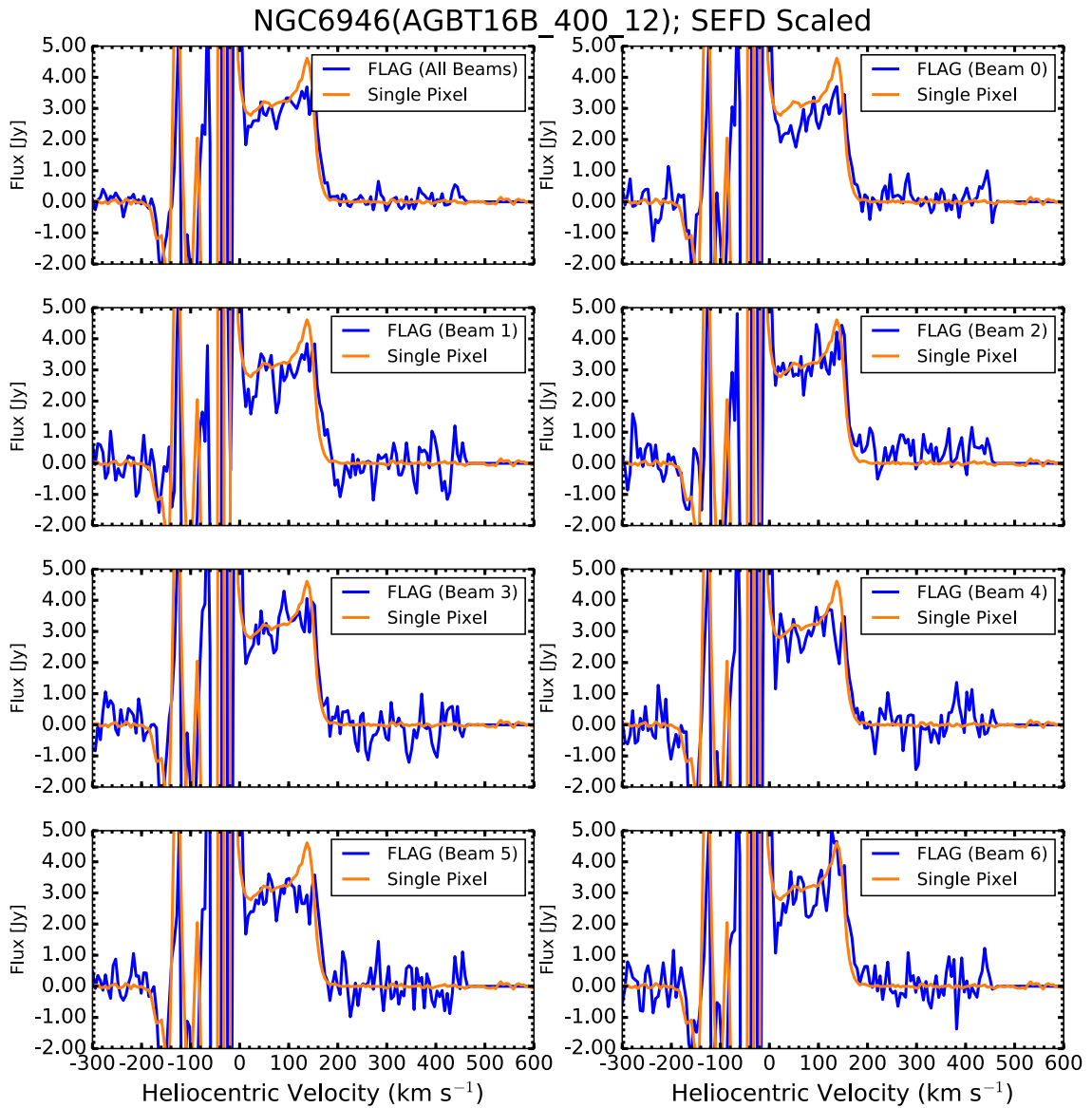


Figure 1.10 HI profiles showing flux as a function of velocity for the combined data set of GBT16B\_400\_12 (LO set at 1450.0000 MHz), in addition to the seven individual beams. All data were scaled by the  $S_{\text{SEFD}}$  for each beam.

NGC6946 (AGBT16B\_400\_13); SEFD Scaled

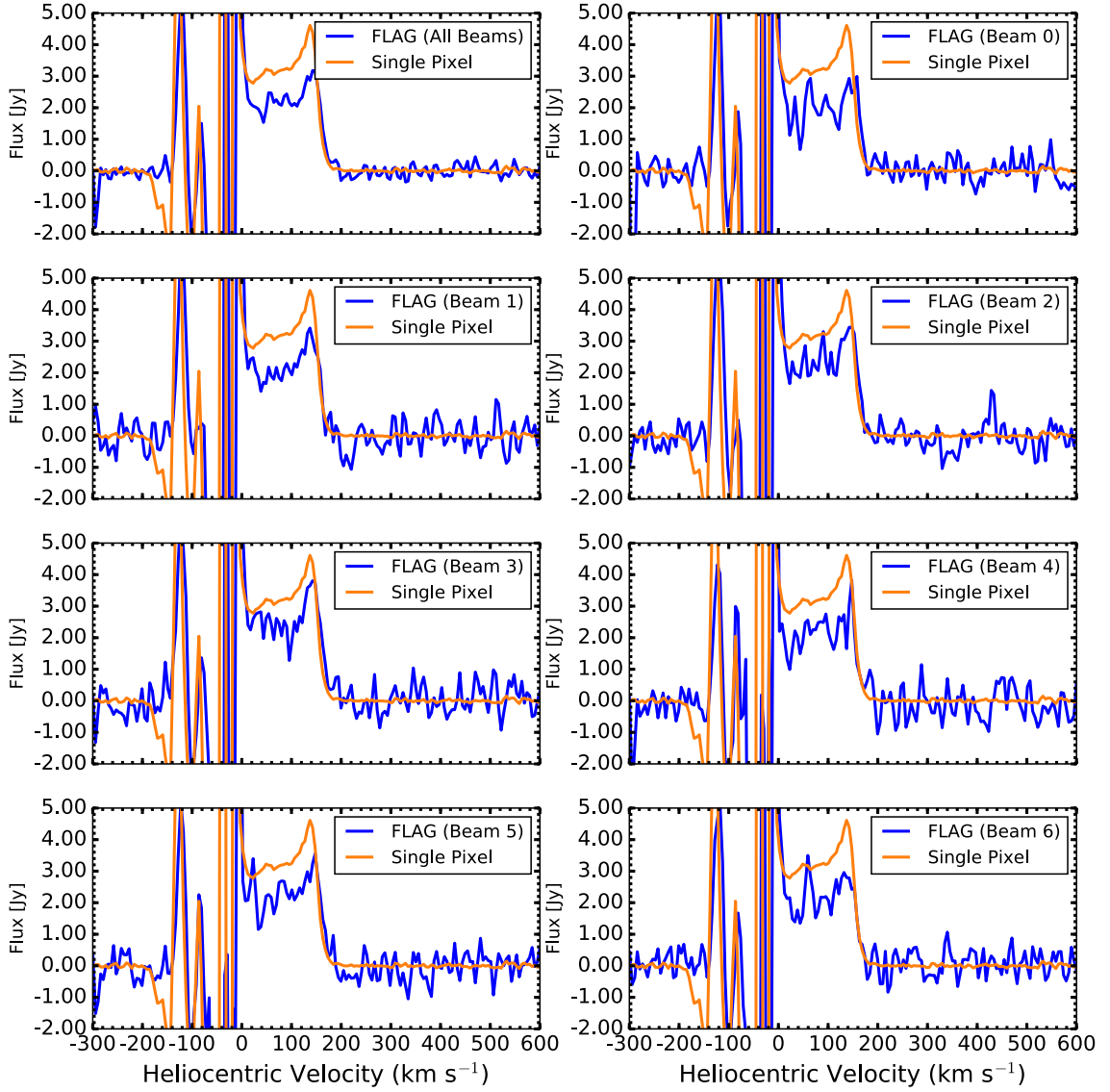


Figure 1.11 HI profiles showing flux as a function of velocity for the combined data set of GBT16B\_400\_13 (LO set at 1449.8484 MHz), in addition to the seven individual beams. All data were scaled by the  $S_{\text{SEFD}}$  for each beam.

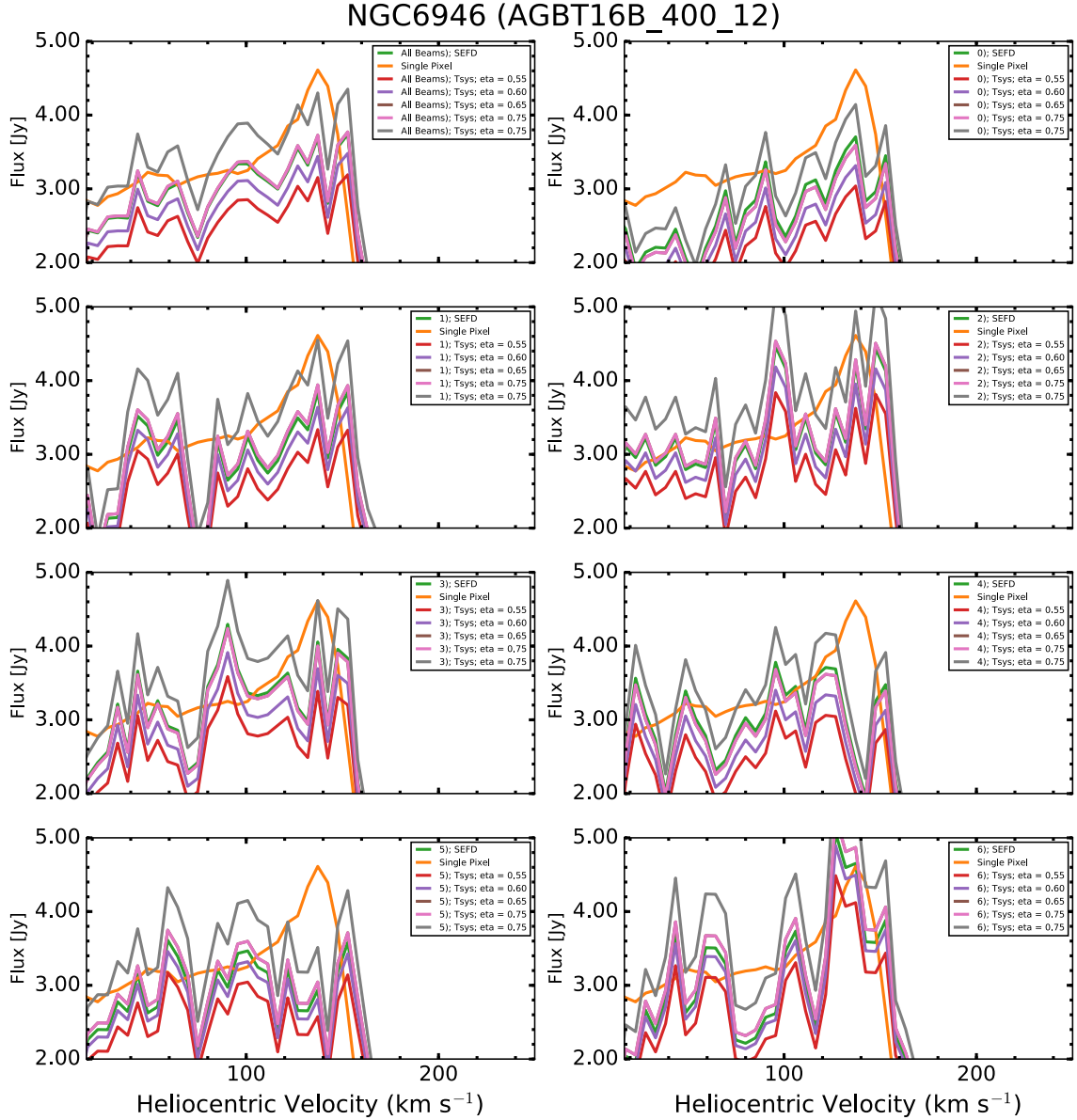


Figure 1.12 HI profiles showing flux as a function of velocity for the data set of GBT16B\_400\_12 where the calibrated data were scaled by the derived  $S_{SEFD}$  (green) and  $T_{sys}/\eta$  varying  $\eta$  from 0.55 (red), 0.60 (purple), 0.65 (magenta), 0.70 (pink), and 0.75 (grey). The single pixel profile is denoted in orange.

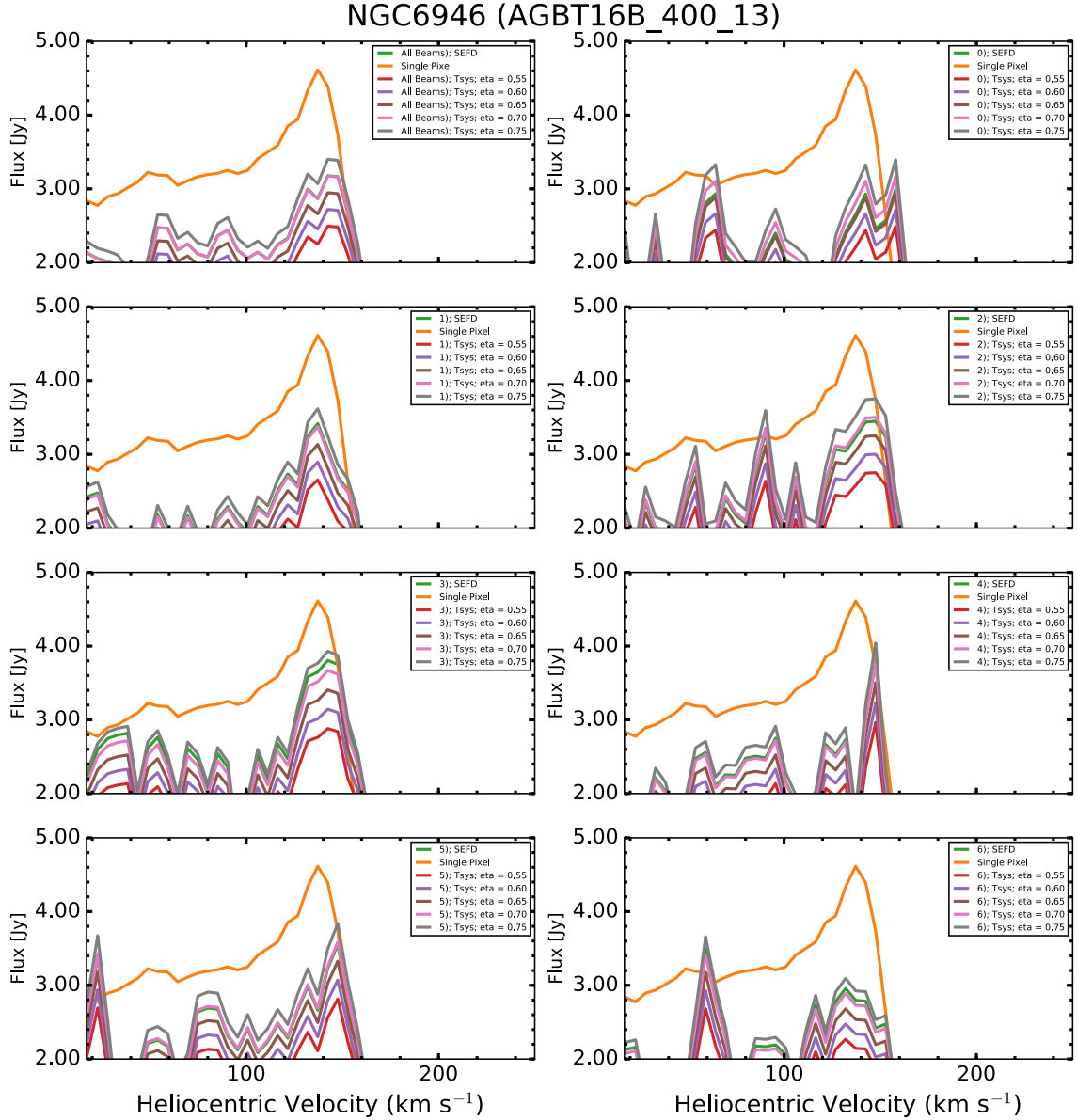


Figure 1.13 HI profiles showing flux as a function of velocity for the combined data set of GBT16B\_400\_13 where the calibrated data were scaled by the derived  $S_{sys}$  (green) and  $T_{sys}/\eta$  varying  $\eta$  from 0.55 (red), 0.60 (purple), 0.65 (magenta), 0.70 (pink), and 0.75 (grey). The single pixel profile is denoted in orange.

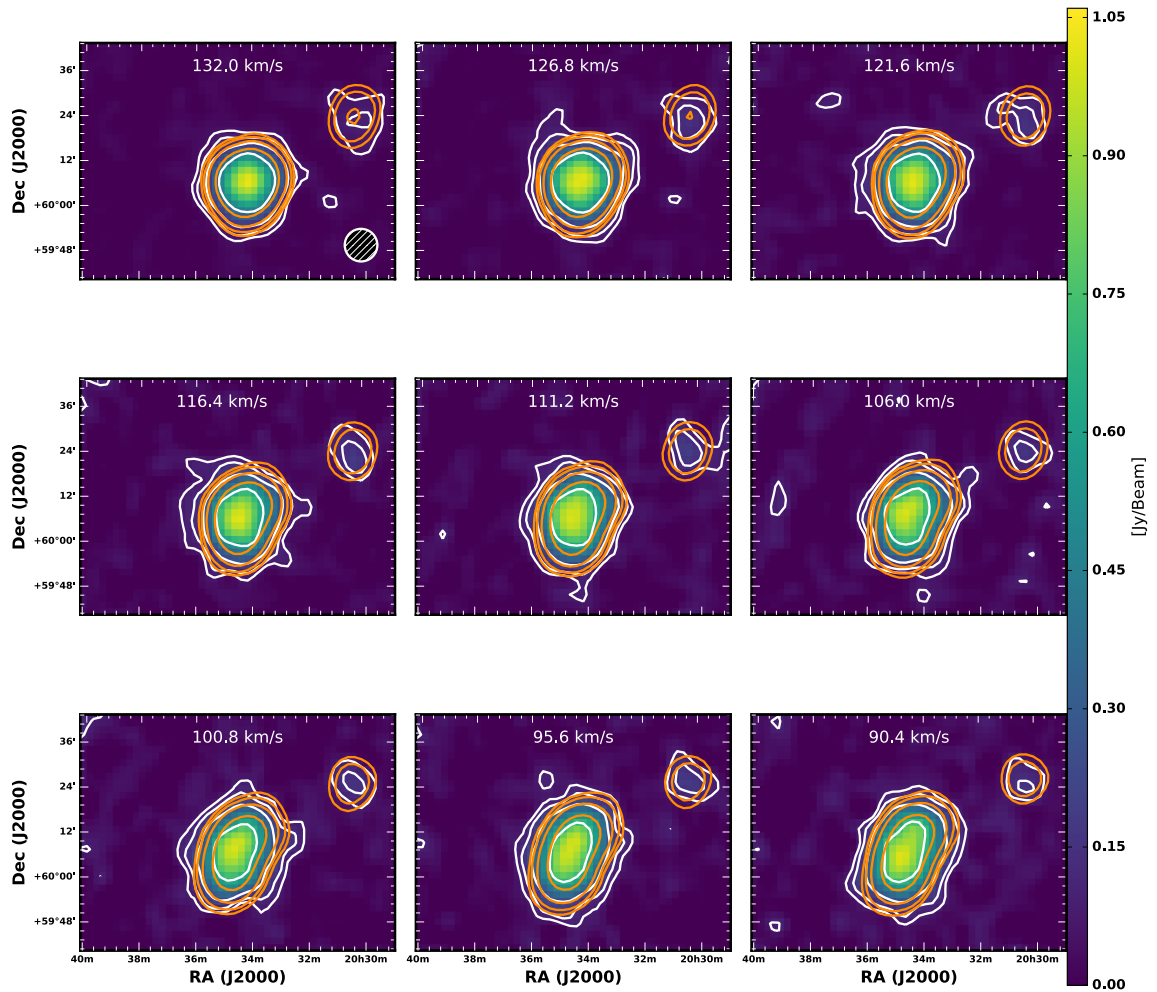


Figure 1.14 Channel maps of the combined data of NGC6946 (all beams from session 12 and 13). In all panels, the color scale and white contours represent the FLAG data, while the orange contours are the single pixel counterpart data set; both sets of contours begin at the 3 times the rms noise of the FLAG data (20 mJy/beam) and continue at 5, 10, and 25 times that level.

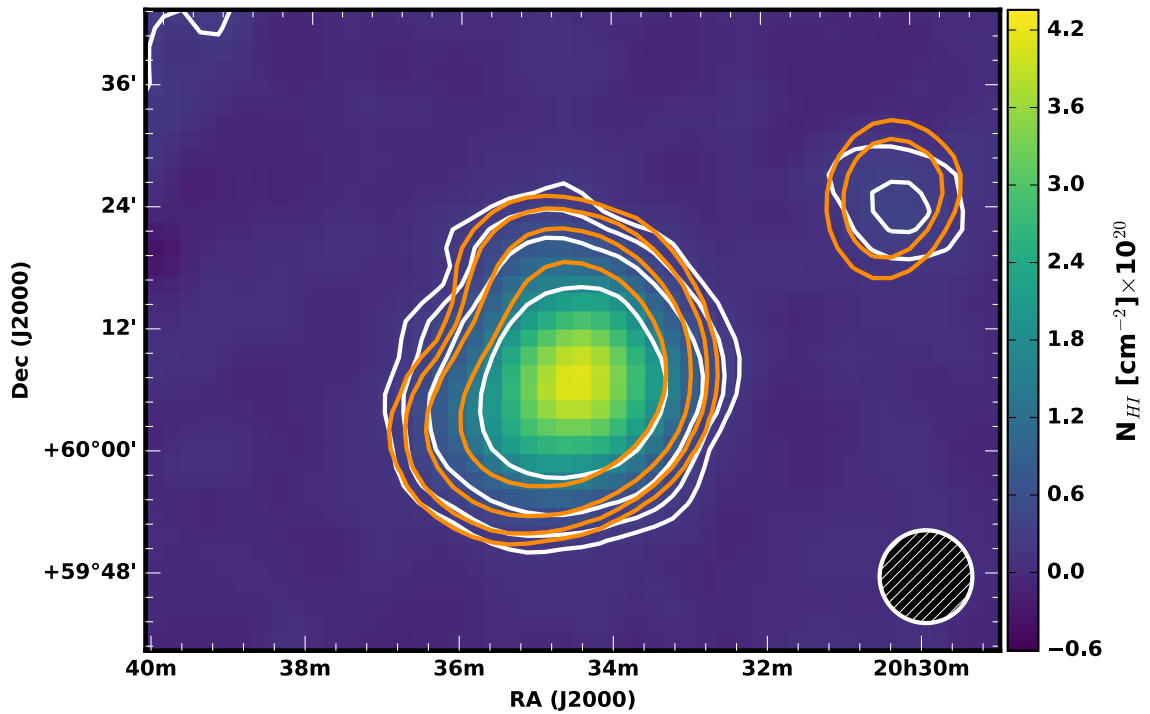


Figure 1.15  $N_{\text{HI}}$  map of NGC6946. Again, the color scale and white contours represent the FLAG data, while the orange contours are the single pixel counterpart data set; both sets of contours begin at the  $-3$  times the  $1\sigma$  uncertainty for the integrated FLAG data set ( $7 \times 10^{18} \text{ cm}^{-2}$ ; dashed lines) of the FLAG data and continue to 3, 5, 10, and 25 times that level (solid lines).

spectively. There is a noticeable discrepancy between the flux profiles of the two data sets and single pixel data. For example, the percent error (taking the single-pixel flux as a ‘theoretical’ value of comparison) in the total flux measured between the velocities of  $18 \text{ km s}^{-1}$  and  $210 \text{ km s}^{-1}$  (to avoid the Galactic HI) for the combined beam data is  $(5.5 \pm 0.4)\%$  for the GBT16B\_400\_12 in Figure 1.10, as opposed to  $(29 \pm 2)\%$  for the equivalent cube for GBT16B\_400\_13 in Figure 1.11. Scale variations in the beamformer weights (see bottom panel of Figure 1.8) could contribute to the large offset. Given the very similar  $S_{\text{SEFD}}$  for each beam between the two sessions (See Table 1.4), using the inverse square of the respective  $S_{\text{SEFD}}$  the weights in the weighted average between the two data sets will inevitably result in a final combined flux profile that is well below that of single pixel profile.

In an attempt to better match the single pixel profile, additional cubes were generated that were scaled with the derived  $T_{\text{sys}}/\eta$  (see column 3 of Table 1.4) instead of  $S_{\text{SEFD}}$ , but assuming various values of  $\eta$  set at 0.55, 0.60, 0.65, 0.70, and 0.75. Zoom-ins of flux profiles that highlight the overall changes are shown in Figures 1.12 and 1.13. In the case of the GBT16B\_400\_12 data, the profile corresponding to  $\eta$  equal to 0.75 initially looks to best match the single pixel profile for all beams. However, when inspecting the integrated flux, the lowest percent error consistently measured over each beam is with the data scaled originally by the derived SEFD.

A large flux discrepancy still exists for the GBT16B\_400\_13 profiles in Figure 1.13 regardless of assumed  $\eta$ . In order to weight the data in a manner that reflects the more consistent flux scaling of the GBT16B\_400\_12 profiles as compared to the reference single pixel profile, the weight coefficients in the weighted average

of the two data sets are the inverse squares of the percent error in total flux measured between  $18 \text{ km s}^{-1}$  and  $210 \text{ km s}^{-1}$  for the data scaled by the SEFD and single pixel data set (with a total flux of  $(474 \pm 24) \text{ Jy km s}^{-1}$ ). These percent errors, along with the total flux values detected for each beam from GBT16B\_400\_12 and GBT16B\_400\_13 are tabulated in Table 1.5; the mean percent error for the seven beams of GBT16B\_400\_12 is  $(5.9 \pm 0.4)\%$ , while increasing to a mean percent error of  $(28 \pm 1)\%$  between beams for GBT16B\_400\_13.

The final profiles of these combined data are shown in Figure 1.16. Due to the larger flux offset in the GBT16B\_400\_13 data, the discrepancies in the final profiles have increased slightly to a mean value of  $(12.7 \pm 0.9)\%$ .

Despite the flux offset, the spatial and spectral agreement between the emission contours in individual channel maps of the final combined cube as shown in Figure 1.15 is very good in general. Discrepancies arise in the lowest contour level, a  $3\sigma$  noise level of  $60 \text{ mJy/beam}$  per channel. This can be attributed to the structure of the sidelobes in the beam-combined cube is very likely complex due to averaging several similar, yet still distinct, aperture illumination patterns as determined by the complex beamformer weights. The agreement along the spectral emission demonstrates that the filler software, `PAF_Filler.py`, correctly performs the conversion from the topocentric to the heliocentric spectral frame.

The contours in the  $N_{\text{HI}}$  image shown in Figure 1.14 also agree well at the high to middle  $N_{\text{HI}}$  levels before slightly deviating as in the individual channels maps at the lowest contour level. Again, this structure can be attributed to the complex sidelobe pattern.

Beam <sup>a</sup>	Flux <sup>b</sup> [Jy km s <sup>-1</sup> ]	Percent Errors <sup>c</sup> [%]
<b>GBT16B_400_12</b>		
Combined	448±22	5.5±0.4
0 (Boresight)	394±20	17±1
1	425±21	10.3±0.7
2	497±25	4.8±0.3
3	473±24	<1
4	394±22	17±1
5	431±22	9.1±0.6
6	475±24	<1
<b>GBT16B_400_13</b>		
Combined	339±17	28±2
0 (Boresight)	310±16	35±2
1	317±16	33±2
2	367±18	23±1
3	397±20	16±1
4	322±16	32±2
5	347±17	27±2
6	316±16	33±2

Table 1.5 Flux Offsets for NGC6946 Data

<sup>a</sup>Formed Beam Number

<sup>b</sup>Total flux in FLAG cube

<sup>c</sup>Percent Error (taking the single-pixel flux of (474±24) Jy km s<sup>-1</sup> as the value of comparison)

NGC6946

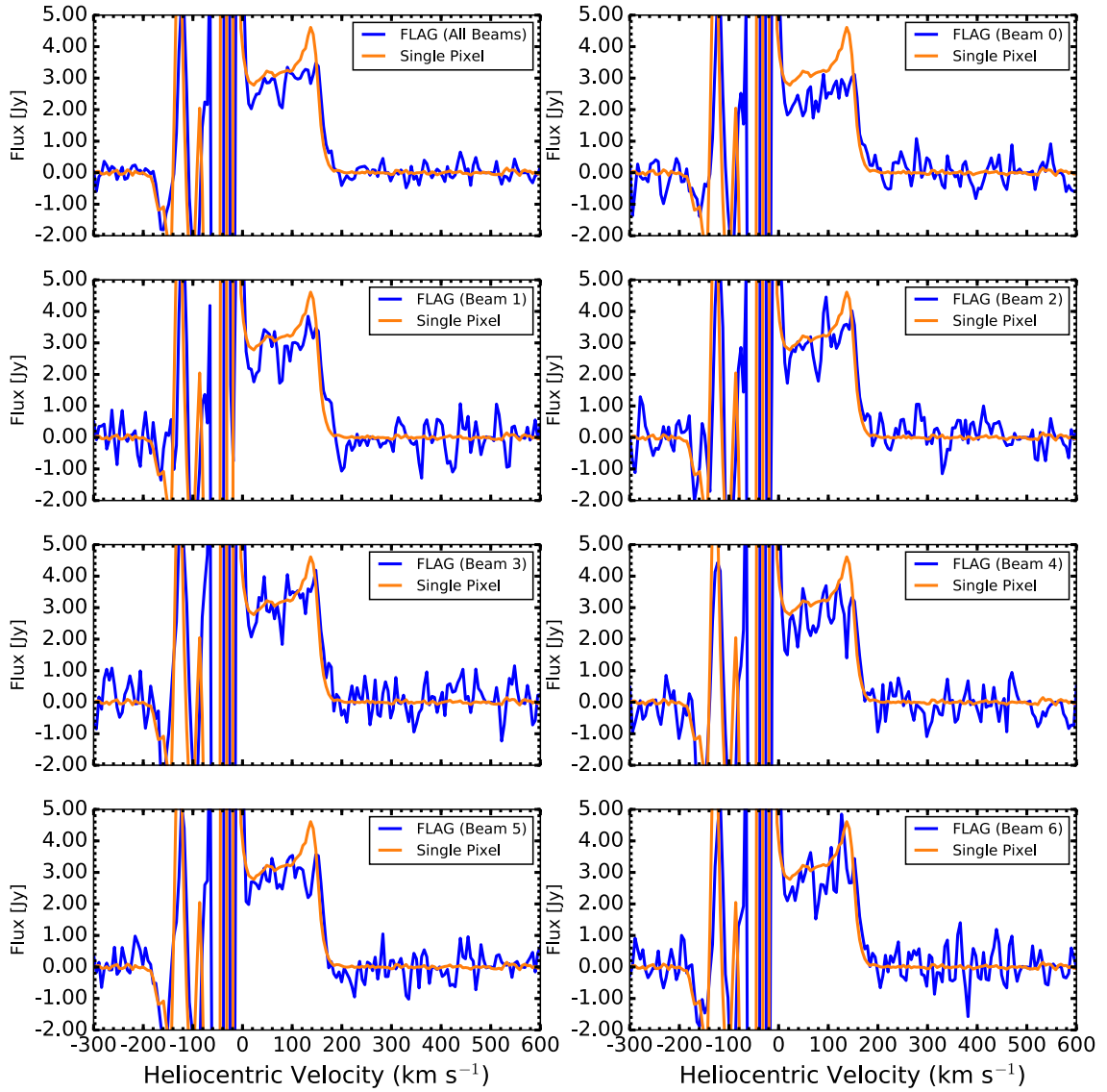


Figure 1.16 HI profiles showing flux as a function of velocity for the combined data set (all beams; top left), in addition to the seven individual GBT beams. All data are from the combination of the the frequency dithered from GBT16B\_400\_12/13.

### 1.5.3.2 M31-M33 Cloud

The HI cloud, M31 Cloud 6, is a discrete structure that exists between the Local Group galaxies M31 and M33 at an adopted distance of 800 kpc (Wolfe et al., 2016). This and several other clouds were first observed at low enough angular resolution enough with the WSRT in total power mode Braun & Thilker (2004) that they resembled a smooth and extended HI feature. The high angular resolution, high velocity resolution, and high sensitivity observations of Wolfe et al. (2013) performed with the GBT resolved the HI into discrete clouds approximately the size of a GBT beamwidth. This particular cloud possesses the highest peak brightness temperature of Wolfe et al. (2016) sample at 80 mK and is an excellent source to test how the measured rms goes with  $t_{\text{eff}}$  for FLAG.

The observations of M31 Cloud 6 consisted of four total on/off pointing pairs with a duration of 5 minutes for each scan. The last pair of on/off pointings are excluded from the remaining analysis due to RFI present in all integrations. Note that due to time constraints, no dithered frequency observation was performed on this source. Seven total beams were formed with the spacing listed in the first two columns of Table 4.4.1. The pointing data for each formed beam were calibrated according to Equations 4.9 and 1.10 and continuum subtracted from a fit to the emission free regions with a 4th order polynomial. The average noise measured over several emission free channels is 6 mJy/beam, which is within 10% of the theoretically predicted noise considering a  $S_{\text{SEFD}}$  of 12 Jy/beam (see Table 1.4),  $\Delta\nu$  of 9.474 kHz, and  $t_{\text{eff}}$  of 7.5 minutes.

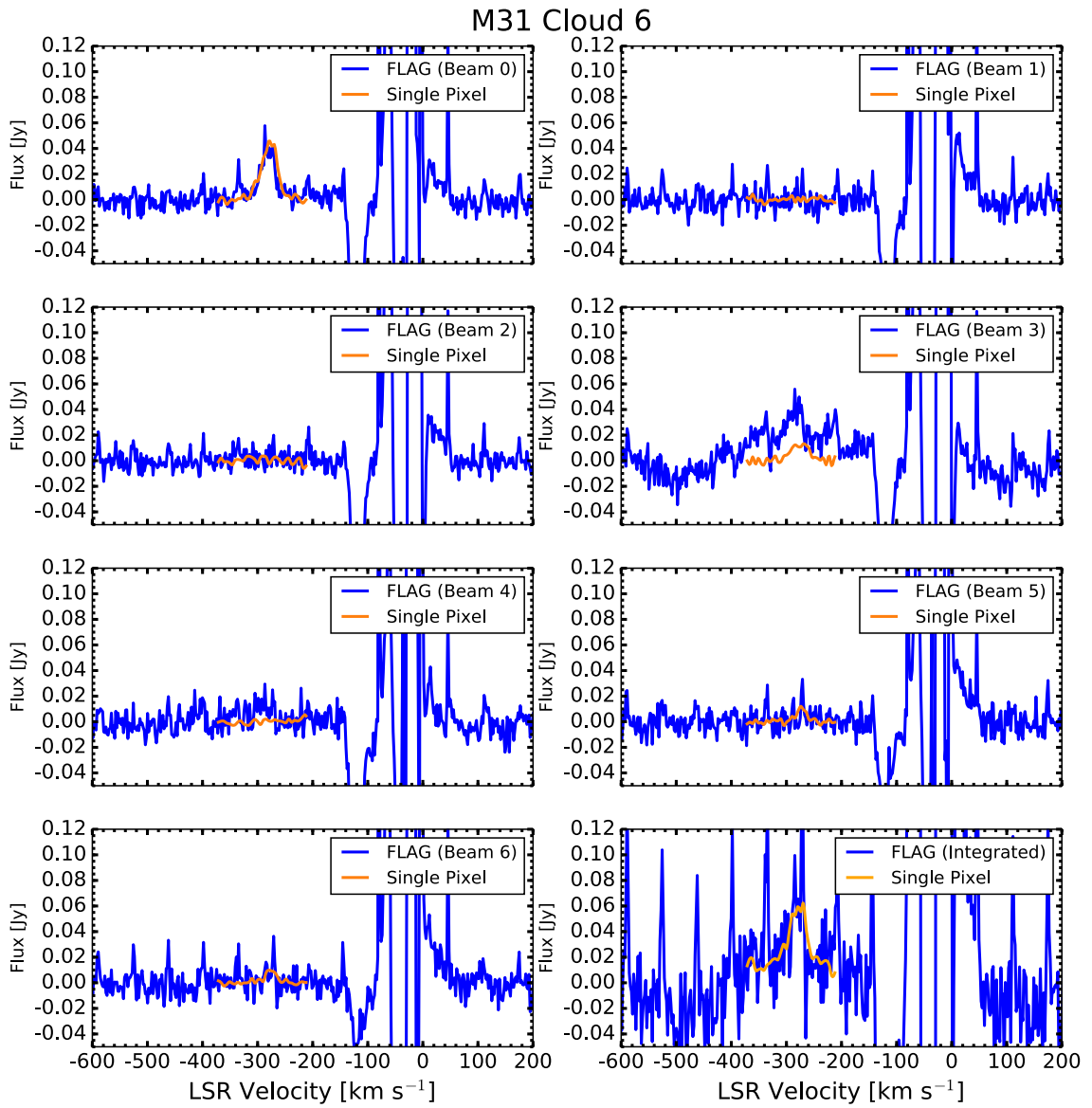


Figure 1.17 HI profiles showing flux as a function of velocity for the individual beams of the pointing towards M31 Cloud 6. The mean spectrum is shown in the lower right panel. The source is only detected in the boresight beam.

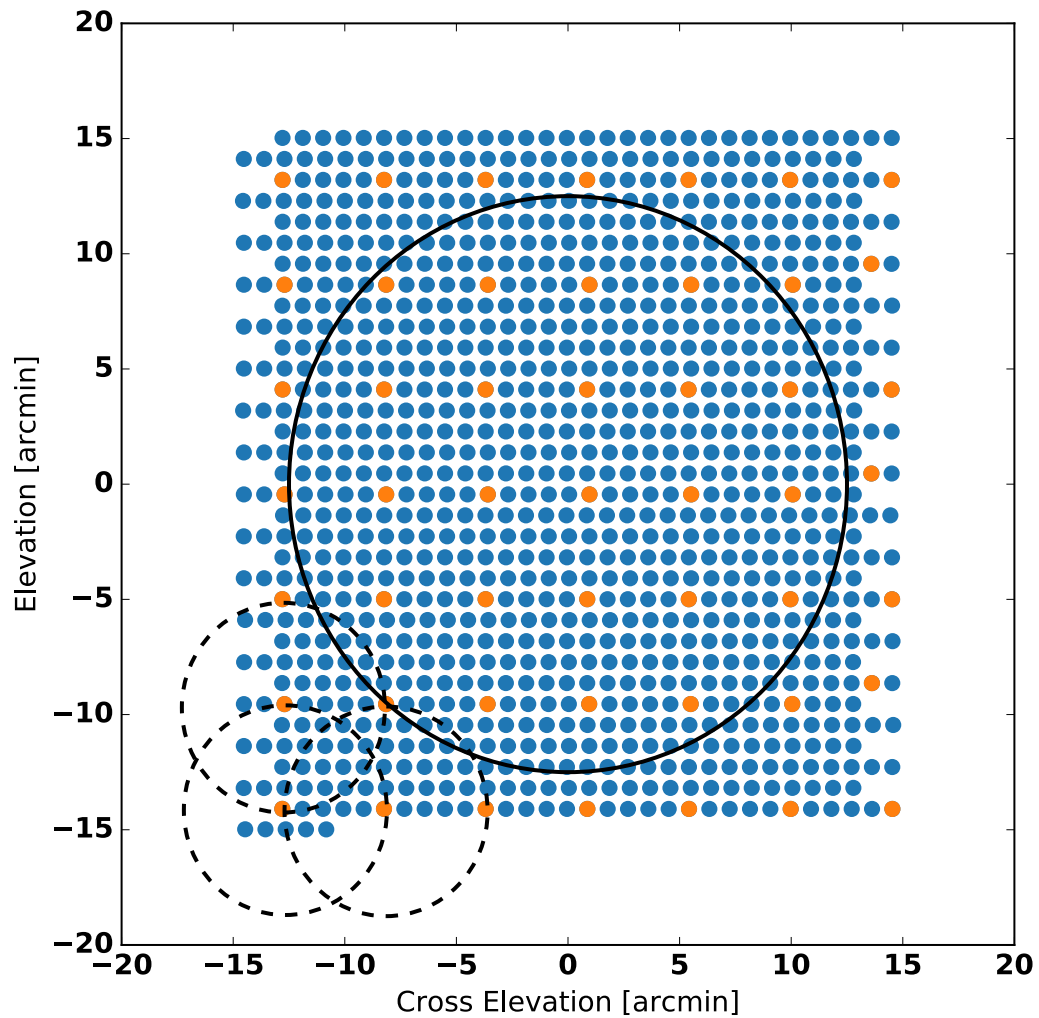


Figure 1.18 The formed beam locations over the PAF FOV (blue circles). The orange circles are the initial beam sample considered for the M31 Cloud 6 ‘snapshot’ map based on the overlap at the half-power point. The orange outside the solid circle were excluded to ensure no loss of sensitivity. The dashed circles give an approximation of the angular widths of each beam.

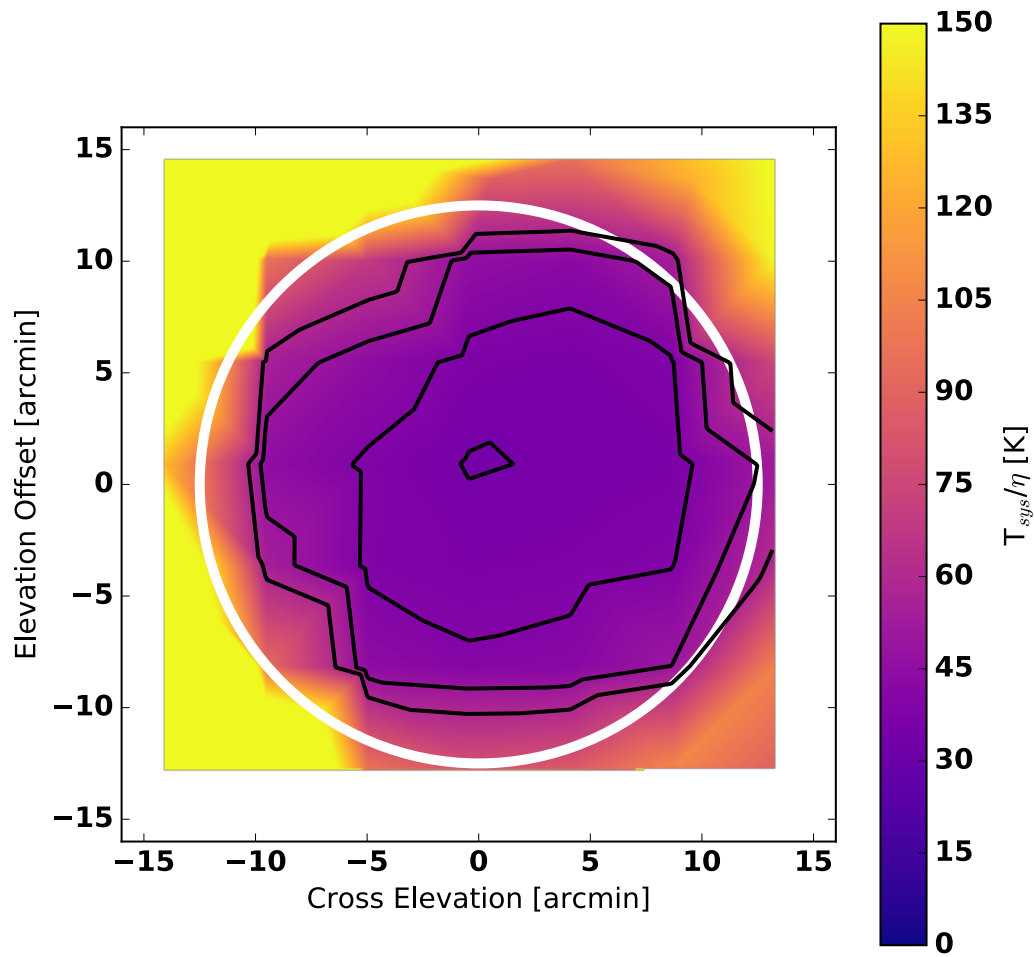


Figure 1.19 The  $T_{\text{sys}}/\eta$  variations across the FOV for the snapshot image of M31 Cloud 6. The central contour level is 30 K and continues at 35, 40, 50, and 60 K. The thick white circle represents the angular threshold outside of which no formed beams were included in the snapshot image.

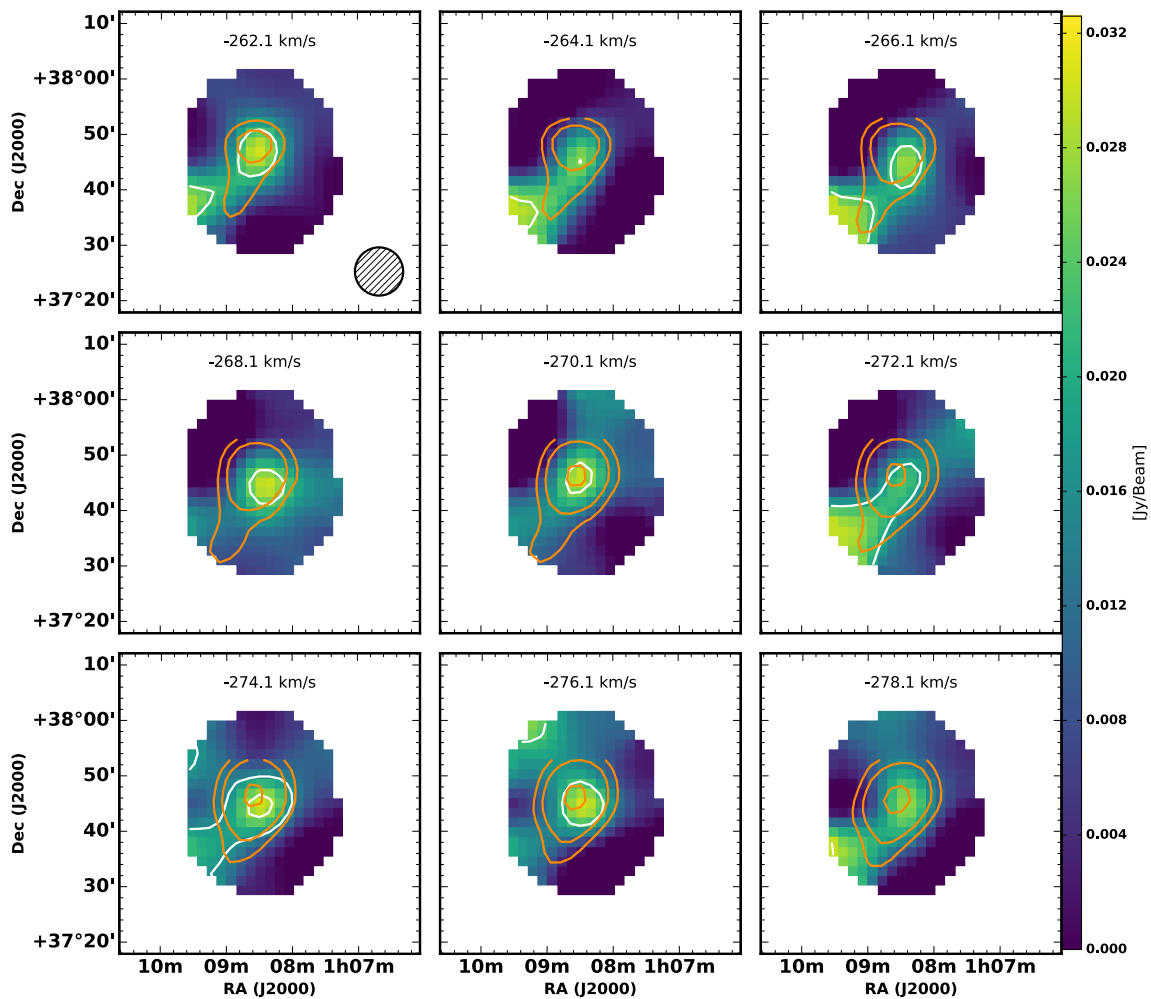


Figure 1.20 Channel maps of the M31 Cloud 6 Snapshot. In all panels, the color scale and white contours represent the FLAG data, while the orange contours are the single pixel counterpart data set; both sets of contours begin at the  $3\sigma$  noise of the FLAG data (14 mK) and continue at 3, 5, and 10 times that level.

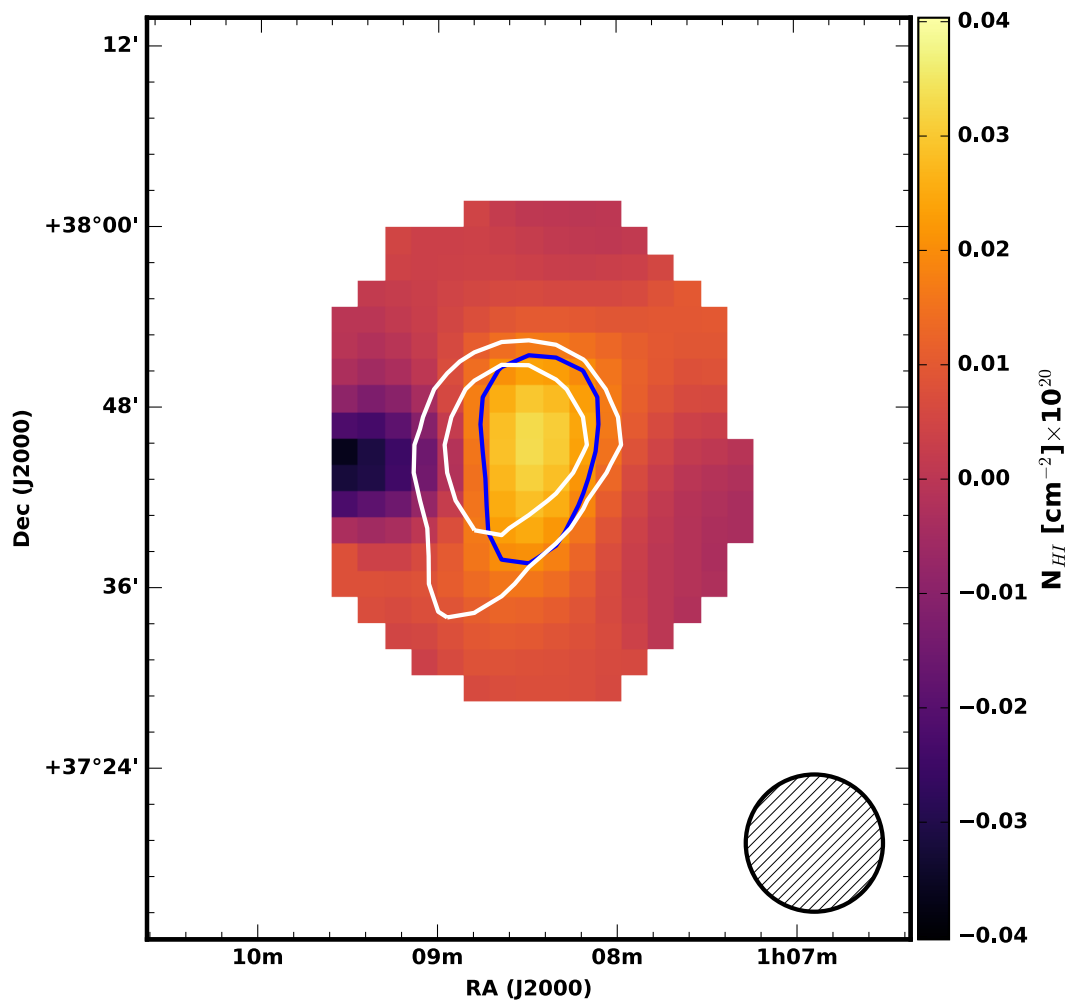


Figure 1.21  $N_{\text{HI}}$  map of the M31 Cloud 6 Snapshot image. The color scale and blue contours represent the FLAG data, while the white contours are the single pixel counterpart data set; both sets of contours begin at the  $3\sigma$  of the FLAG data set ( $2 \times 10^{18} \text{ cm}^{-2}$ ) and continue to 3 and 5 times that level.

Figure 1.17 shows these calibrated spectra for each individually formed beam (blue) with the spectra taken from the location of the formed beam center in the single-pixel data cube (orange). The lower right panel shows the average spectrum of the seven formed beams. The source is only detected in the boresight beam, which is unsurprising given the half-power points of the formed beams were not overlapping during the 16B\_400 observing run. The peak fluxes between the boresight spectrum and the single-pixel data match excellently. Additionally, the total flux detected in the boresight beam as determined by the integral between LSR velocities of  $-320$  to  $-245$  km s $^{-1}$  is  $(1.60 \pm 0.13)$  Jy km s $^{-1}$ , which matches the single pixel value of  $(1.63 \pm 0.04)$  Jy km s $^{-1}$  within the statistical uncertainties.

There are some aspects of these spectra that emphasize issues with the system that need to be addressed in the future. For one, the apparent detection in Beam 3 is due to residual baseline structure. Even more pertinent are the artifacts caused by the scalloping that show up as spurious features seen in all individual beam spectra. Their presence explicitly demonstrates the necessity of implementing a revised PFB scheme in the PFBCORR mode to mitigate influence of the scalloping on the calibrated data. That said, the clear detection of M31 Cloud 6 in the boresight beam, and the excellent noise properties as compared to theoretical expectations further establishes the feasibility of using FLAG to study faint HI sources at unprecedented levels.

Recall that correlation matrices characterizing the noise in the system and a signal are necessary for electronically forming a beam on the sky. A calibration grid procedure as described in Section consists of  $\sim 1000$  ‘signal’ integrations over

the  $30 \times 30$  deg<sup>2</sup> FOV traced out by the grid trajectory. In principle, if the nearest dedicated ‘Off’ pointing is used to obtain a noise correlation matrix, a beam can be formed at each of signal integrations resulting in a ‘snapshot’ of the sky intensity made with many hundreds of beams. Such an imaging technique would be beneficial for obtaining images of compact ( $\lesssim 20'$ ), but still extended enough ( $> 9'$ ) to be resolved, sources within the FLAG FOV.

Beamformer weights were generated using the calibration grid of 3C147 for session GBT16B\_400\_14. Again, the spectra were calibrated according to Equations 4.9 and 1.10, but instead of seven total SDFITS files, a total of 1028 beams are available. The pointing centers of these beams are shown as circular blue points in Figure 1.18. Not all beams need to be used, however. The dashed circles in Figure 1.18 show the approximate beam width for several individual formed beams. The overlap from individual beams would lead to significant oversampling. The layout of the beams selected for imaging is such that the FOV has beams overlapping at their half-power points. The beams that fit this criteria are filled in with orange in Figure 1.18. There is still concern about the potentially steep drop in sensitivity towards the edge of FOV, which will contribute image artifacts near the edge of the FOV. The  $T_{\text{sys}}/\eta$  for each beam is interpolated to a grid and shown in Figure 1.19. The variation across the image is moderately uniform within the central region up to about  $12'$  in radius before sharply increasing due to the loss response from dipoles that cannot see the point calibration source. To ensure the beams included in the final image do not suffer from degradation due to loss of sensitivity, only the beams within the spatial boundary denoted by the solid circles in Figures 1.18 (solid black)

and 1.19 (solid white) are include in the final image. The data were imaged using the GBO pipeline task `gbtgridder`<sup>6</sup> with a Gaussian-Bessel convolution function, 105  $\square''$  pixels, with a spatial extent of 128 $\times$ 128 pixels.

Individual channel maps are shown in Figure 1.20. The channel maps show reasonable agreement between the contours of the FLAG and single-pixel data sets in most channels, although clear artifacts towards the edge of the FOV still have signatures that extend into the central region to affect the source emission. The  $N_{\text{HI}}$  image in Figure 1.21 reveals the artifact more clearly, indicating it is likely a product of degraded beamformer towards the edge of the FOV. That said, the contours tracing integrated emission from the two data sets match reasonably well at the faintest of  $N_{\text{HI}}$  levels. The generally good spatial agreement of the emission contours across multiple intensity levels over a diameter of  $\sim 20'$  demonstrates that this imaging mode has potential.

## 1.6 Conclusions, Current Status and Future

The spectral line commissioning results and derived system properties of a new beamformer for FLAG, a cryogenically cooled PAF for the GBT, were presented.

The main conclusions from these initial data are:

- Custom software written to convert the raw correlation matrices to beamformed spectra that can be used in the GBO computing environment by the application of complex beam weights works as intended. The conversion, or ‘fill-

---

<sup>6</sup><https://github.com/nrao/gbtgridder>

ing’, software is available at <https://github.com/nipingel/SpectralFiller>.

- FLAG is most sensitive between the topocentric frequencies of 1200 MHz up to about 1500 MHz as revealed by the frequency sweep observation. The mean  $T_{\text{sys}}/\eta$  derived for all beams over all observing runs is consistent with the existing single pixel L band receiver, agreeing with the conclusion of Roshi et al. (2018) that FLAG is currently the world’s most sensitive PAF.
- On-the-fly maps of the external galaxy NGC6946 show equivalent  $t_{\text{eff}}$  can be reached about seven times faster due to the increased FOV provided by FLAG over the single pixel receiver.
- Comparisons between FLAG maps and equivalent maps made with the single-pixel receiver show reasonable agreement in terms of the spatial contours of the emission — albeit noisier at the lowest statistically significant emission levels due to higher sidelobe levels in the formed beams. The source of the  $\sim 30\%$  flux offset in each beam as compared to equivalent single-pixel data still needs to be determined.
- The overall phase of the derived complex beamforming weight vectors does not vary much over timescales of  $\sim 1$  week. However, the amplitude of the weights can vary largely between independent sessions on the timescale of days. The large spread in amplitude, while not detrimental to the overall sensitivity, will cause considerable gain variations across the FOV and introduce make flux scale matching between sessions.

- A position switched observation of a faint HI cloud reveals a clear detection in the boresight beam, verifying the capabilities of FLAG to probe low  $N_{\text{HI}}$  levels in extragalactic sources. An experimental snapshot image, where  $\sim 45$  beams were simultaneously formed over the FOV of FLAG shows reasonable agreement with the single-pixel data both on a channel by channel comparison and for intensity integrated along the spectral axis. That said, due to a sharp decrease in sensitivity towards the edge of the FOV care must be taken to select the spatial layout of the beams; that is, only select beams that overlap at the half-power point within inner  $\sim 20'$ ). A snapshot imaging mode would be advantageous for acquiring images of objects smaller than about  $20'$  in extent, either through position switching or daisy mapping.
- Scalping artifacts in fine channel mode, originating from the current implementation of the PFB, cause spurious spikes in the calibrated bandpass. While these can be mitigated by shifting the LO by one half of a coarse channel (i.e., 151.18 kHz) to create a frequency dithered image, the combination of these data introduces several additional calibration steps.

Given its status as the world's most sensitive PAF, FLAG will provide the GBT with a clear advantage over existing large single dish telescopes in terms of HI survey speeds and help to ensure that it remains a premiere instrument for radio astrophysics. Open issues remain, however, that must be addressed to ensure reliable performance over observation sessions spread over multiple days. Firstly, the scalping introduced by the current PFB implementation will be completely miti-

gated in the next iteration of the backend software set to be written in the Summer of 2018. Secondly, individual threads handling one-twentieth of the bandpass simply die during a scan, which causes — in some cases — multiple missing chunks of spectra. These dropouts cause discontinuous spectra. The issue seems to be related to the efficiency of the current GPU codes and is a priority going forward. Finally, the loss of beamformer weight validity whenever the LO is changed due to loss of word/bit lock contributes to increased overhead. Good beamformer weights can be achieved within about 5 to 10 minutes through the use of 7-point calibration scans, but it is still imperative that overhead is reduced

Although there are several moderate backend issues to be addressed before FLAG becomes a publicly available receiver for the GBT, the commissioning results presented in this chapter clearly establish it among the premiere PAFs currently in operation on large radio telescopes and primed to become a shared risk instrument. Results of the science mapping observations taken during Winter 2018 observing run (GBT17B\_360, GBT17B\_455, and GBT17B\_360) to be presented in future publications show promising steps towards the reduction of overhead, observations of Galactic sources, and further sensitivity improvements. The future of FLAG — and PAFs in general — to provide expedited mapping times of diffuse  $N_{\text{HI}}$  and is extremely promising.